Resource

Cell

A High-Throughput Platform to Identify Small-Molecule Inhibitors of CRISPR-Cas9

Graphical Abstract

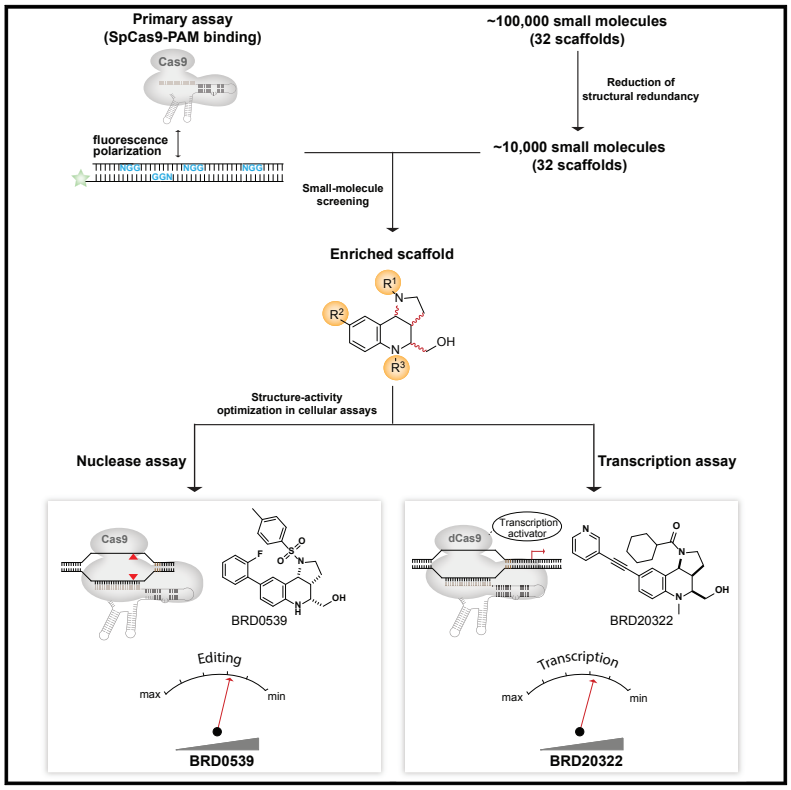

Highlights

- Developed high-throughput assays for SpCas9 and performed a small-molecule screen
- Identified reversible and cell-permeable inhibitors that disrupt SpCas9-DNA binding
- Inhibitors allow dose and temporal control of (non)-nuclease-based SpCas9 systems
- Identified a pharmacophore for SpCas9 inhibition using structure-activity studies

Authors

Basudeb Maji, Soumyashree A. Gangopadhyay, Miseon Lee, ..., Paul A. Clemons, Bridget K. Wagner, Amit Choudhary

Correspondence

achoudhary@bwh.harvard.edu

In Brief

A suite of high-throughput assays enables discovery of small-molecule inhibitors of CRISPR-Cas9 that are cell permeable, and non-toxic, providing a chemical means to control SpCas9-based tools.

Maji et al., 2019, Cell *177*, 1067–1079
May 2, 2019 Published by Elsevier Inc.
https://doi.org/10.1016/j.cell.2019.04.009

CellPress

Cell

A High-Throughput Platform to Identify Small-Molecule Inhibitors of CRISPR-Cas9

Basudeb Maji,[1,2,3] Soumyashree A. Gangopadhyay,[1,2,3,10] Miseon Lee,[1,2,10] Mengchao Shi,[1,2,3,10] Peng Wu,[1,2,3,10] Robert Heler,[4] Beverly Mok,[5,6] Donghyun Lim,[1,2] Sachini U. Siriwardena,[1] Bishwajit Paul,[1,2,3] Vlado Dančík,[1] Amedeo Vetere,[1] Michael F. Mesleh,[7] Luciano A. Marraffini,[4,8] David R. Liu,[5,6,9] Paul A. Clemons,[1] Bridget K. Wagner,[1] and Amit Choudhary[1,2,3,11,*]

[1]Chemical Biology and Therapeutics Science Program, Broad Institute of MIT and Harvard, Cambridge, MA 02142, USA
[2]Department of Medicine, Harvard Medical School, Boston, MA 02115, USA
[3]Divisions of Renal Medicine and Engineering, Brigham and Women's Hospital, Boston, MA 02115, USA
[4]Laboratory of Bacteriology, The Rockefeller University, New York, NY 10065, USA
[5]Merkin Institute of Transformative Technologies in Healthcare, Broad Institute of Harvard and MIT, Cambridge, MA 02142, USA
[6]Department of Chemistry and Chemical Biology, Harvard University, Cambridge, MA 02138, USA
[7]Center for the Development of Therapeutics, Broad Institute of MIT and Harvard, Cambridge, MA 02142, USA
[8]Howard Hughes Medical Institute, The Rockefeller University, 1230 York Avenue, New York, NY 11231, USA
[9]Howard Hughes Medical Institute, Harvard University, Cambridge, MA 02138, USA
[10]These authors contributed equally
[11]Lead Contact
*Correspondence: achoudhary@bwh.harvard.edu
https://doi.org/10.1016/j.cell.2019.04.009

SUMMARY

The precise control of CRISPR-Cas9 activity is required for a number of genome engineering technologies. Here, we report a generalizable platform that provided the first synthetic small-molecule inhibitors of *Streptococcus pyogenes* Cas9 (SpCas9) that weigh <500 Da and are cell permeable, reversible, and stable under physiological conditions. We developed a suite of high-throughput assays for SpCas9 functions, including a primary screening assay for SpCas9 binding to the protospacer adjacent motif, and used these assays to screen a structurally diverse collection of natural-product-like small molecules to ultimately identify compounds that disrupt the SpCas9-DNA interaction. Using these synthetic anti-CRISPR small molecules, we demonstrated dose and temporal control of SpCas9 and catalytically impaired SpCas9 technologies, including transcription activation, and identified a pharmacophore for SpCas9 inhibition using structure-activity relationships. These studies establish a platform for rapidly identifying synthetic, miniature, cell-permeable, and reversible inhibitors against both SpCas9 and next-generation CRISPR-associated nucleases.

INTRODUCTION

SpCas9 is a programmable RNA-guided DNA endonuclease from *S. pyogenes* that has allowed the facile introduction of genomic alterations. The complex of SpCas9 and guide RNA (gRNA) recognizes a substrate sequence via a protospacer adjacent motif (PAM) and base-pairing of the target DNA with gRNA (Chen and Doudna, 2017). The ease of targeting catalytically impaired SpCas9 to any genomic locus has resulted in transformative technologies (Komor et al., 2016; Wang et al., 2016). For example, the fusion of catalytically inactive SpCas9 (dCas9) to transcriptional activators or repressors has enabled gene transcription and repression; the fusion of catalytically impaired SpCas9 to base-modifying enzymes has allowed base conversion (e.g., C→T) at specific genomic sites, a dCas9–GFP fusion has made the imaging of genomic loci possible, and dCas9–acetyltransferases or deacetylases fusion has enabled epigenome editing.

The need for precision control of both wild-type and engineered SpCas9 over the dimensions of dose and time has created a demand for inhibitory anti-CRISPR molecules (Nuñez et al., 2016). SpCas9 is being developed as a gene therapy agent for multiple pathologies, including HIV, muscular dystrophy, and vision and hereditary disorders (Cox et al., 2015; Fellmann et al., 2017). Dose and temporal controls, which are required of all therapeutic agents, are particularly important for SpCas9, as off-target effects, chromosomal translocations, and genotoxicity are observed at elevated activity (Gangopadhyay et al., 2019). Indeed, the timely and partial inhibition of SpCas9 selectively diminishes off-target editing events over on-target ones (Shin et al., 2017). Furthermore, temporal control is important because most delivery systems use constitutively active SpCas9, and this activity must ideally be terminated following on-target editing (Gangopadhyay et al., 2019).

SpCas9 inhibitors will be useful in several other contexts. First, in germline editing, restricting SpCas9 activity to a narrow temporal window is important, as persistent activity in dividing cells contributes to mosaicism (Wang et al., 2013; Yen et al., 2014). Timely SpCas9 degradation reduced mosaicism in non-human primate embryos (Tu et al., 2017). Second, temporarily switching

off gene drives that propagate lethal traits using a SpCas9 inhibitor (Champer et al., 2016; Esvelt et al., 2014; Gantz and Bier, 2016) will allow facile animal husbandry and population expansion for field studies. Furthermore, dose and temporal control of gene drives in a laboratory setting will allow precision population control and propel our understanding of the limits of this technology. Third, inhibiting SpCas9-mediated toxicity to helper cells can enable the efficient packaging of SpCas9 in adeno-associated viruses for delivery (Neve et al., 2005). Fourth, SpCas9 inhibitors could help allay dual-use concerns, where research that is designed to provide a benefit could be co-opted to do harm, from a biosafety perspective in the use of SpCas9 in disease modeling (Wegrzyn et al., 2017). Fifth, SpCas9 inhibitors will propel the fundamental understanding of the biological functions of endogenous SpCas9 and can apply immune-response-based selection pressure on bacteria to evolve new CRISPR-based systems. Finally, dCas9-based technologies, including base editing, will benefit from dose and temporal control.

While several protein-based anti-CRISPR molecules have been reported (Hynes et al., 2017; Pawluk et al., 2016a, 2016b; Rauch et al., 2017; Shin et al., 2017), we focused on small molecules as they complement the protein-based anti-CRISPRs in multiple ways. For example, small-molecule inhibitors can be cell permeable, reversible, proteolytically stable, and non-immunogenic, while protein-based anti-CRISPRs can be highly potent, since they generally possess a greater number of SpCas9 interaction sites. Unlike genetic methods used to express protein-based anti-CRISPRs, small-molecule inhibitors exhibit fast kinetics, inhibiting enzymatic activity in as little as a few minutes (Weiss et al., 2007) and allowing precise temporal control. Small molecules can be synthesized on a large scale at low cost, with little batch-to-batch variability. Unsurprisingly, the pharmacological inhibition of intracellular proteins is usually accomplished using small molecules. Unfortunately, the identification of small-molecule inhibitors of SpCas9 is challenging for multiple reasons. First, inhibitor identification requires robust, orthogonal, sensitive, high-throughput, miniature, and inexpensive SpCas9 assays, which are currently unavailable (Cox et al., 2019). Second, SpCas9 is a single-turnover enzyme that holds on to its substrate with picomolar affinity throughout the biochemical reaction (Sternberg et al., 2014), adding to the challenge of developing such high-throughput assays. Third, the inhibition of SpCas9 activity requires the inactivation of two nuclease domains. Fourth, SpCas9 possesses novel protein folds, limiting the ability to leverage existing rational design approaches (Nishimasu et al., 2014). Finally, SpCas9 is a DNA-binding protein, a class of targets that are often deemed chemically intractable (Koehler, 2010).

Here, we describe a platform for the rapid identification and validation of small-molecule inhibitors of SpCas9. We developed a suite of high-throughput assays for SpCas9 activity, including a fluorescence-polarization-based primary screening assay for probing the SpCas9-PAM interaction. Using this primary screening assay, we sampled a set of small-molecule libraries derived from diversity-oriented synthesis (DOS) (Schreiber, 2000) to identify specific libraries enriched for screening hits. A focused screen of the enriched libraries resulted in the identification of BRD0539 as a SpCas9 inhibitor. We exhaustively validated the activity of BRD0539 in multiple biochemical and cell-based assays and demonstrated target engagement by BRD0539 in cells. Furthermore, BRD0539 is stable in human plasma and reversibly inhibits SpCas9. Finally, we performed structure-activity and stereochemistry-activity relationship studies for BRD0539 to identify its inactive analogs and the pharmacophore required for SpCas9 inhibition. These studies lay the foundation for the rapid identification of cell-permeable, reversible, synthetic anti-CRISPR molecules for contemporary and emerging CRISPR-associated nucleases.

RESULTS

Development of High-Throughput Primary and Secondary Assays

Primary Assay for SpCas9-PAM Binding

We focused on targeting the SpCas9-PAM interaction for several reasons. Mutating the PAM binding site renders SpCas9 inactive (Kleinstiver et al., 2015a), and disrupting PAM binding has been exploited by numerous anti-CRISPR proteins. Furthermore, SpCas9 has a low affinity for the PAM sequence that can be effectively blocked by small molecules. We used fluorescence polarization (FP) to monitor the interaction between SpCas9 and a fluorophore-labeled, PAM-containing, DNA oligonucleotide. The binding of a small-sized PAM-rich DNA to a much larger SpCas9:gRNA complex lowers DNA's tumbling rate, with a concomitant increase in anisotropy (Figure 1A). However, the low-affinity SpCas9-PAM interaction creates a challenge in developing robust binding assays, as the interaction is not strong enough to make a sustained, measurable change in the anisotropy that is detectable over background. To overcome this challenge, we employed a DNA sequence bearing multiple PAM sites (henceforth called 12PAM-DNA) that should increase the association between the DNA and the SpCas9 (Table S1). As expected, the binding of SpCas9:gRNA to 12PAM-DNA resulted in a dose-dependent increase in FP (Figure 1B). We confirmed the PAM dependence of SpCas9:gRNA and 12PAM-DNA interactions in competition experiments using unlabeled DNA sequences containing a varying number of PAM sites. As expected, the decrease in FP of 12PAM-DNA correlated with the density of PAM sites on the competitor DNA (Figure 1C) as well as with the concentration of the competitor DNA. Next, we used differential scanning fluorimetry (DSF), which detects ligand-induced changes in protein stability. The melting temperature of the SpCas9:gRNA complex increased with the number of PAM sites in the DNA sequence (Figure 1D). Finally, using bio-layer interferometry (BLI) (Richardson et al., 2016), we confirmed the increased affinity of SpCas9:gRNA for DNA sequences containing more PAM sites (Figure 1E; Table S1).

Secondary Assays for Cell-Based SpCas9 Activity

We developed several cell-based, orthogonal, and high-throughput assays of SpCas9 activity using either gain or loss of signal. Joung and co-workers previously reported a U2OS.eGFP.PEST cell line in which *eGFP* knockout by SpCas9 led to a loss of fluorescence (Fu et al., 2013; Kleinstiver et al., 2015a); in this cell line, the percentage of eGFP-negative cells correlates with SpCas9 activity. Using automated imaging and counting of eGFP-positive cells, we adapted this

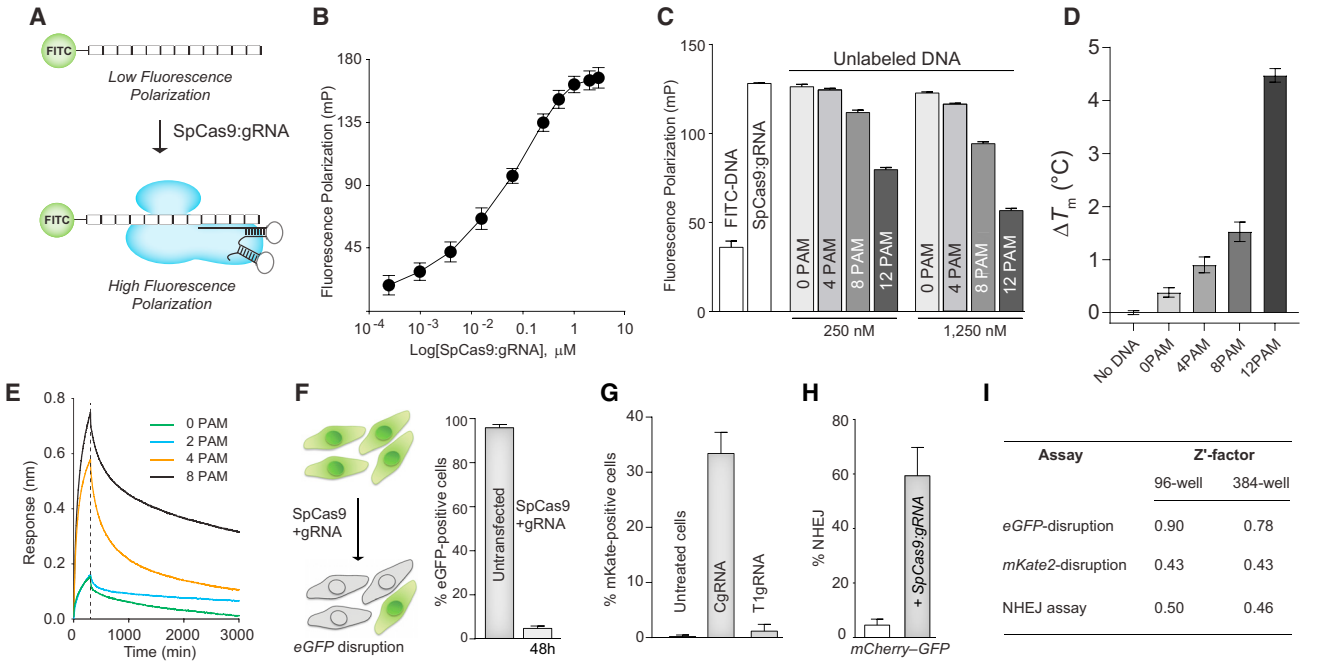

Figure 1. Development of a Screening Workflow for Identification of SpCas9 Inhibitors

(A) Schematic representation of the FP assay for monitoring SpCas9:gRNA and DNA binding.

(B) Dose-dependent increase in the FP signal upon binding of 12PAM-DNA to the SpCas9:gRNA complex. Error bars represent ±SD across technical replicates (n = 3).

(C) Competition experiment demonstrating PAM-specific DNA-SpCas9:gRNA binding wherein 0–12 PAM refers to unlabeled competitor DNA containing the indicated number of PAM sequences. Unlabeled competitor DNA was used in two different ratios: 10 × (250 nM) and 50 × (1,250 nM). Error bars represent ±SD across technical replicates (n = 3).

(D) Differential scanning fluorimetry (DSF) assay showing an increase in the thermal stability of the SpCas9:gRNA complex upon binding to DNA containing an increasing number of PAM sequences. Error bars represent ±SD across technical replicates (n = 3).

(E) Representative BLI sensogram showing the interaction of SpCas9:gRNA with *ds*DNA containing a variable number of PAM sequences. Streptavidin sensors were loaded with 300 nM biotin-*ds*DNA with a variable number of PAM sequences, and the interaction was followed by incubating with 200 nM SpCas9:gRNA complex. Data are for one of the two replicates.

(F) Schematic representation of the eGFP-disruption assay involving the quantification of eGFP disruption by SpCas9 at 48 h post-nucleofection. U2OS.eGFP.PEST cells were nucleofected with SpCas9 and gRNA plasmids followed by incubation for 48 h before imaging. Error bars represent ±SD across technical replicates (n = 4).

(G) Quantification of mKate2-disruption assay in HEK293T cells. Cells were transfected with a plasmid encoding the *mKate2* reporter, SpCas9, and either a non-targeting guide (CgRNA plasmid) or a targeting guide (T1gRNA plasmid). Cells transfected with the CgRNA plasmid showed a high number of mKate2-positive cells, while cells transfected with the T1gRNA plasmid showed a significant reduction in the number of mKate2-positive cells 48 h after transfection. Error bars represent ±SD across technical replicates (n = 4).

(H) Quantification of non-homologous end joining (NHEJ) assay in HEK293T cells. SpCas9-induced NHEJ was quantified by measuring mCherry and GFP expression in HEK293T cells after 48 h. Cells were transfected with the reporter construct encoding either the mCherry-Stop codon (TAG)-GFP, SpCas9, and gRNA or the reporter construct alone. GFP fluorescence observed in the cells transfected with only the reporter indicates the basal level of NHEJ. The GFP fluorescence increases significantly in cells transfected with the reporter, SpCas9, and gRNA indicating an increase in NHEJ following *ds*DNA break by SpCas9. Error bars represent ±SD across technical replicates (n = 4).

(I) Z′-factor values for cell-based secondary assays (eGFP disruption, mKate2 disruption, and NHEJ) in two different plate formats. Assays were performed in 16 technical replicates for 48 h.

See also Figure S1 and Table S1.

eGFP-disruption assay in a 96-well or 384-well format with a $Z' = 0.9$ or 0.8, respectively (Figures 1F and 1I; Figures S1A and S1D) (Zhang et al., 1999). In a second fluorescence-based assay, we used HEK293T cells expressing a single plasmid construct (Cas9-mKate2-gRNA) encoding both SpCas9 and gRNA components along with their red fluorescent protein target *mKate2* (Figures 1G and S1B) (Moore et al., 2015). We quantified the SpCas9-triggered loss of mKate signal using automated microscopy, yielding an assay with $Z' = 0.5$ in a 96-well format (Figures 1I and S1D). These two assays, when deployed for inhibitor identification, are gain-of-signal assays that have a lower probability of false positives. We complemented these assays with a loss-of-signal, non-homologous end joining (NHEJ) assay in which cells are transfected with two plasmids in an equimolar ratio: one plasmid expressing out-of-frame *eGFP* downstream of *mCherry*, with the two separated by a stop codon, and the other plasmid expressing SpCas9 and a gRNA that can target the stop codon linker, bringing the *eGFP* gene in-frame (Nguyen et al.,

2016). In this assay, SpCas9-mediated DNA cleavage induced eGFP expression, affording an assay with a $Z' = 0.4$ in a 96-well format (Figures 1H and 1I; Figures S1C and S1D). Unlike the mKate2 assay, we can use mCherry expression in this assay to normalize for transfection efficiency.

Small-Molecule Screening and Identification of Enriched Libraries

Our initial primary screen focused on a 2,652-membered performance-diverse compound collection (Wawer et al., 2014) containing 2,240 small molecules from commercial libraries and 412 from DOS-derived libraries. All screening hits in this experiment were DOS compounds (data not shown). Indeed, DOS libraries of natural-product-like compounds have performed well against microbial targets (Comer et al., 2014; Gerry and Schreiber, 2018). However, screening all available 100,000 DOS compounds across 32 libraries would be inefficient, as compounds *within* a single library are structurally similar and may perform similarly in assays. Instead, we employed a computational approach to assemble 9,549 compounds, a DOS "informer set," which maximally represented the structural diversity across all DOS compounds (Figure S1E). We screened the DOS informer set using the FP assay (Figure 2A), employing 12PAM-DNA lacking a fluorophore as a positive control. Screening hits, which lowered the FP signal by $>3\sigma$ compared to the DMSO vehicle-control distribution, were grouped by library to assess the enrichment (Figure 2B; Table S2). Members of the Pictet-Spengler, spirocyclic azetidine, and Povarov libraries (Comer et al., 2015; Gerard et al., 2012) yielded screening hit rates >1%.

Biochemical and Cellular Validation of the Povarov Scaffold

We chose not to pursue the spirocyclic azetidine library, as the compounds lowered the FP of 12PAM-DNA in the absence of SpCas9:gRNA, suggesting non-specificity (data not shown). Screening additional members of the Pictet-Spengler and Povarov libraries using the FP assay and subsequent counterscreening revealed that most Pictet-Spengler compounds, but not Povarov compounds, exhibited significant fluorescent background, and the hits from the Pictet-Spengler library were also cytotoxic (Figures 2C and S2A). As such, before embarking on activity-guided structure optimization in cells, we decided to validate the binding and inhibitory activity of the Povarov scaffold using small molecules BRD7087 and BRD5779 and their biotinylated analog BRD3539 (Figure S2B). BLI studies using BRD3539 and the SpCas9:gRNA complex suggested a dissociation constant of 0.7 μM (Figures 2D and S2C). No detectable binding was observed in the absence of the Povarov scaffold or in the presence of a 10-fold excess of biotin (Figures S2D and S2E). After confirming that BRD7087 was soluble up to 75 μM in PBS (Figures S2F and S2G), we used ^{19}F NMR spectroscopy to validate the binding of BRD7087 to SpCas9:gRNA. We observed a differential line broadening of the ^{19}F signal upon titration with SpCas9:gRNA (Figure 2E; Table S3; Figure S2H), with significant broadening occurring at protein concentrations as low as 0.75 μM (67-fold excess of BRD7087), indicating tight binding. We confirmed that BRD7087 and BRD5779 were non-cytotoxic (Figures S2I and S2J), demonstrated dose-dependent inhibition of SpCas9 in the eGFP-disruption assay (Figures 2F, S2K, and S2L), and found BRD7087 to inhibit SpCas9 up to ~44% at 10 μM without either affecting eGFP expression (Figure S2M) or inducing notable auto-fluorescence (Figure S2N). BRD7087 and BRD5779 showed a dose-dependent inhibition of SpCas9 in both the mKate2 disruption (Figures S2O and S2P) and NHEJ assays (Figure S2Q). Since BRD7087 and BRD5779 alter PAM binding, they may inhibit technologies that use a catalytically impaired SpCas9, including transcription activation and base editing. The dose-dependent inhibition of dCas9-based transcription activation of *HBG1*, but not of the control gene, was observed using BRD7087 and BRD5779, attaining ~60% inhibition of transcriptional activation at 20 μM (Figures 2G and S2R). Both compounds also inhibited C→T conversion of the *EMX1* gene using the SpCas9(A840H)-cytidine deaminase conjugate (BE3) (Komor et al., 2017; Rees et al., 2017), with close to a 2-fold reduction in C→T conversion at 20 μM (Figure S2S).

Cell-Based Activity-Guided Structure Optimization Identifies BRD0539 as a SpCas9 Inhibitor

Upon biochemical and cellular validation of the Povarov scaffold, we sought to improve the potencies of the identified SpCas9 inhibitors in mammalian cells. To this end, we tested 641 structural analogs of BRD7087 (either synthesized or available from the Broad Institute) at 15 μM in the cell-based eGFP-disruption assay, and several compounds possessed greater potency than BRD7087 (Figure 3A; Table S4). Our hit-triage workflow involved prioritizing compounds based on the absence of cytotoxicity and the presence of dose-dependent inhibition in the eGFP-disruption assay when SpCas9 was provided to the cells as a ribonucleoprotein complex or as a plasmid. From these studies, BRD0539 and BRD3433 emerged as top performers with a 1.8-fold improvement in potency over BRD7087 in the eGFP-disruption assay (Figures 3B–3D and S3A) and an apparent EC_{50} of 11 μM. To confirm that these SpCas9 inhibitions were independent of the DNA repair mechanisms or the optical readout, we employed a HiBiT assay (Schwinn et al., 2018). While the eGFP-disruption assay is a fluorescence-based assay involving error-prone DNA repair, the HiBiT assay involves SpCas9-mediated homology-directed tagging of GAPDH with a short peptide, which produces luminescence upon complementation with a subunit derived from nanoluciferase (Figure 3E). Both compounds exhibited dose-dependent inhibition of SpCas9 in the HiBiT assay with BRD0539 being more active. The inhibitory activity of BRD0539 was further confirmed using fluorescent-activated sorting of eGFP cells (Figure S3B), real-time monitoring of eGFP disruption (Supplementary Videos 1–3 in https://doi.org/10.17632/jpxvnh3n2t.1), the surveyor assay, and next-generation sequencing of the *eGFP* locus (Figures S3C, 3F, S3D). We note that, while BRD0539 is cell permeable, protein-based anti-CRISPRs (e.g., AcrIIA4) are not and require delivery methods like nucleofection (Figure 3G). To demonstrate the reversible inhibition of SpCas9 by BRD0539, we performed eGFP-disruption experiments wherein cells were treated with short pulses of BRD0539 followed by treatment with inhibitor-free media. The cells with media swap at an earlier time point

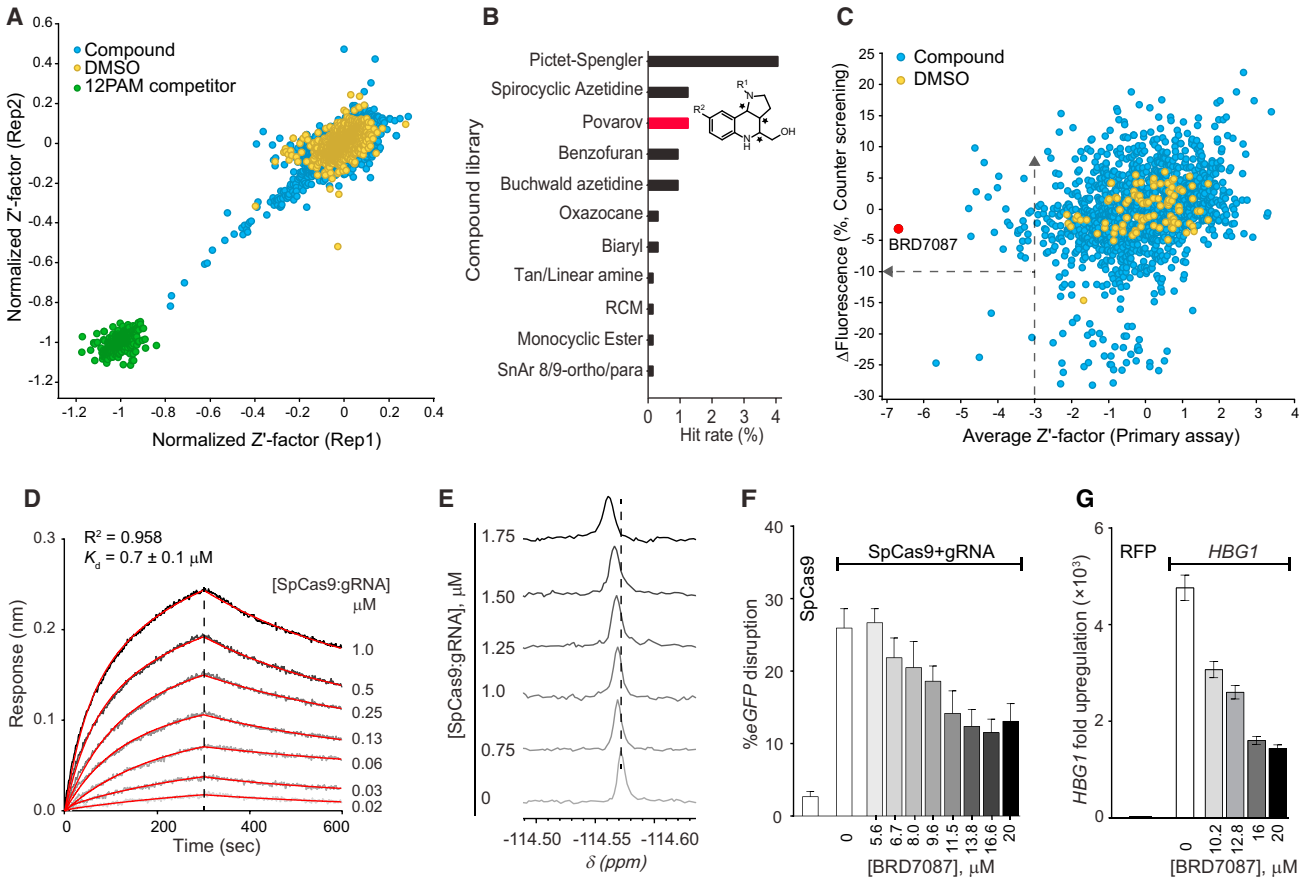

Figure 2. High-Throughput Screening and Identification of Inhibitor Scaffold

(A) Screening results of FP-based assay against 9,549 DOS compounds. Dots in yellow, blue, and green represent DMSO controls, small molecules, and unlabeled 12PAM competitor, respectively.

(B) Hit-rate distribution across the DOS informer set in the FP-based primary assay.

(C) Screening and counterscreening results against the Povarov library. Dots in yellow and blue represent DMSO controls and small molecules, respectively. BRD7087 is indicated in red.

(D) BLI measuring small-molecule binding with the SpCas9:gRNA complex. Streptavidin sensors were loaded with 1 μM of BRD3539, and the interaction was followed by varying the SpCas9:gRNA complex from 0.15 to 1 μM. Global fitting of the response curves against ribonucleoprotein concentration provided the dissociation constant (Figure S2C).

(E) Binding interaction of the BRD7087 and SpCas9:gRNA ribonucleoprotein complex probed via ^{19}F NMR spectrometry. Line broadening in the ^{19}F peak signal indicates the association of BRD7087 with SpCas9.

(F) Dose-dependent inhibition of SpCas9 by BRD7087 in U2OS.eGFP.PEST cells. Compound was tested from 5 to 20 μM. U2OS.eGFP.PEST cells were nucleofected with SpCas9- and gRNA-expressing plasmids and incubated with the compound at the indicated concentration for 24 h before imaging. Error bars represent ±SD across technical replicates (n = 4). *p ≤ 0.0001 for the small molecule at 20 μM compared to DMSO (unpaired t test, two-tailed)

(G) Dose-dependent inhibition of dSpCas9-based transcriptional activation of *HBG1* in HEK293FT cells. Cells were transfected with dSpCas9, MS2.p65.HSF1.GFP, and either *RFP* or *HBG1* plasmids and were incubated in the presence of the small molecule at the indicated concentrations before processing for RT-qPCR. The experiments were performed in three biological replicates, and each biological replicate was processed in six technical replicates. The data represent mean ± SEM for technical replicates. *p ≤ 0.0001 for the small molecule at 20 μM compared to DMSO (unpaired t test, two-tailed).

See also Figures S1 and S2, Tables S1 and S2, and Data S1.

had lower levels of eGFP disruption, suggesting reversible inhibition by BRD0539 (Figure 3H). In contrast, the SpCas9 inhibition by AcrIIA4 was irreversible (Figure 3H). We confirmed binding of the identified compounds to SpCas9:gRNA using BLI (Figures S3E and S3F) following the aforementioned protocol. BRD0539 exhibited a dose-dependent inhibition (apparent IC_{50} = 22 μM) in an *in vitro* DNA cleavage assay, even when the concentration of SpCas9 (5 nM) was much higher than typically present in cells (Figures 3I and S3G). Finally, we confirmed that none of the compounds were auto-fluorescent in cells, none were cytotoxic to multiple cell lines or primary cells (Figures S3H–S3J; Supplementary Item 1 in https://doi.org/10.17632/jpxvnh3n2t.1), and all the compounds were stable in human plasma (Figure 3J) (Di et al., 2005).

Structure-Activity Relationship of BRD0539

To identify the pharmacophore of BRD0539, we examined the activities of structural analogs that differed in R^1 or R^2 groups

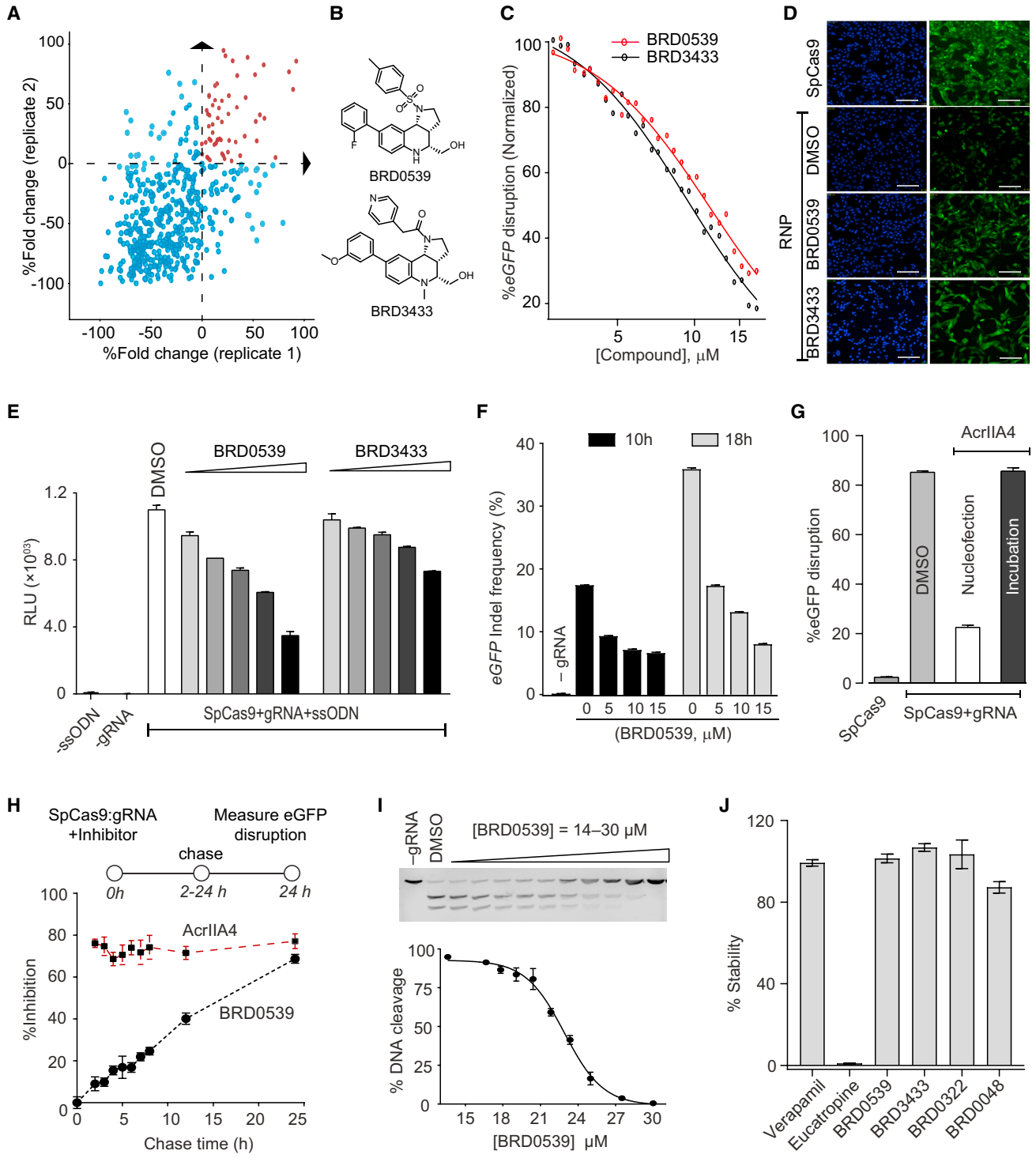

Figure 3. Identification and Validation of Small-Molecule Inhibitors of SpCas9

(A) Scatterplot of activity of BRD7087 analogs in the eGFP-disruption assay. U2OS.eGFP.PEST cells were nucleofected with SpCas9- and gRNA-expressing plasmids and incubated with 15 μM of the compounds for 24 h before imaging. The top-right quadrant represents the compounds with an activity higher than that of BRD7087 in both replicates.

(B) Chemical structures of inhibitors BRD0539 and BRD3433.

(C) Dose-dependent inhibition of SpCas9 by BRD0539 and BRD3433 in U2OS.eGFP.PEST cells with an EC_{50} of 11.5 and 9.3 μM, respectively. Inhibitors were tested from 2.8 to 17.3 μM. U2OS.eGFP.PEST cells were nucleofected with either SpCas9 or preformed SpCas9:gRNA ribonucleoprotein complex and incubated

(legend continued on next page)

but not both (Figure 4A). Keeping R^2 = a and varying R^1 showed that sulfonamides (1–4) were more potent than amides (5–7), perhaps because a sulfonamide can accept two hydrogen bonds while an amide can only accept one. Interestingly, minor changes on R^1 significantly altered the potencies—while 1, 2, or 3 have similar bond connectivity except for the nature of the substituent at the para-position, replacing the methyl group (1) with a fluoro (2) or methoxy (3) group decreased the activity by 18% and 20%, respectively. Furthermore, altering the position of the methyl group from para- (1) to meta- (4) resulted in a 47% reduction in activity. Introducing heteroatoms on the rings (5–8) failed to improve potency—the compound with R^1 = 8 was virtually inactive. Keeping R^1 = 1 and varying R^2 groups showed that alkynl spacers (b or d) lowered the inhibitory activity, which was also observed for an alkenyl moiety. Substituting the relatively small 2-fluoro- (a) with the larger 3-*N,N*-dimethyl-carbamoyl (c) group also led to the loss of activity. We compared the activity of BRD0539 at 12 different dose points in the eGFP-disruption assay with that of BRD3497 and BRD9419, which have a 4-methyl-imidazole or a 2-keto-pyridyl group, respectively, in place of the *p*-tolyl group in BRD0539. While BRD0539 showed dose-dependent inhibitory activity, BRD3497 and BRD9419 barely inhibited SpCas9 (Figures 4B and 4C; Supplementary Videos 4–8 in https://doi.org/10.17632/jpxvnh3n2t.1). The lower inhibitory activity of BRD3497 and BRD9419 was apparent in the HiBiT assay, as well, where BRD0539 showed a greater than 2-fold higher activity (Figure 4D).

In addition to the aforementioned structure-activity relationship, we determined the stereochemical structure-activity relationship for BRD0539 by testing the activities of four stereoisomers in the eGFP-disruption assay (Figures 4E and S4A). Interestingly, among the four stereoisomers, BRD0539 with *RRR* stereochemistry was the most potent, pointing to the specific nature of interactions between SpCas9 and BRD0539. Finally, we also observed some structure-activity relationship with BRD3433. Keeping R^2 = a and systematically varying R^1 showed that the size and nature of the R^1 rings are important: compounds with substituents containing a pyridine (1) or phenyl ring (2,3) are more active than compounds with an imidazole ring (4 or 5), a cyclobutane ring (8), or a benzo[*d*][1,3] dioxole ring (7) (Figure S4B). Furthermore, compounds with aryl rings at R^1 were better inhibitors than those with an aliphatic ring—the compound with R^1 = 8 was virtually inactive. In contrast to BRD0539, introducing a heteroatom on the ring improves the potency (R^1 = 1 versus R^1 = 3). Finally, replacing the aryl ring with bromine led to a drastic 78% reduction in activity.

Mechanism of Inhibition and Specificity of BRD0539

To determine whether BRD0539 disrupted the binding of gRNA to SpCas9, we developed and utilized a FP assay for SpCas-gRNA binding. We monitored the binding of fluorescein isothiocyanate-labeled (FITC)-crRNA:tracrRNA to SpCas9 using FP, observing a sharp increase in the polarization signal upon the addition of SpCas9 to the gRNA (Figure 5A). While the addition of unlabeled competitor gRNA (1 equiv.) caused a drop in polarization signal (Figure 5B), the addition of BRD0539 did not perturb the polarization signal, suggesting that BRD0539 does not interfere with the SpCas9:gRNA interaction (Figure 5C).

Next, we examined whether BRD0539 disrupted the interactions of SpCas9 with DNA using DSF. Briefly, the melting curves of SpCas9 lacking the gRNA (*apo*-SpCas9) suggested the presence of a DNA-bound state upon the addition of DNA with

with the inhibitors at the indicated concentrations for 24 h before imaging. Error bars represent ±SD across technical replicates (n = 3). *p ≤ 0.0001 for both small molecules at 15 μM compared to DMSO (unpaired t test, two-tailed).

(D) Representative images of the eGFP-disruption assay. U2OS.eGFP.PEST cells were nucleofected with either SpCas9 alone (untreated) or preformed SpCas9:gRNA ribonucleoprotein complex and were treated with the vehicle alone or inhibitors BRD0539 and BRD3433 at 15 μM for 24 h. Left and right panels represent DAPI and GFP channels, respectively.

(E) Dose-dependent inhibition of SpCas9 by BRD0539 and BRD3433 in the HiBiT assay. Inhibitors were tested from 6 to 20 μM. U2OS.eGFP.PEST cells were nucleofected with SpCas9- and gRNA-expressing plasmids along with the single-stranded oligodeoxynucleotides (ssODN) containing the HiBiT tag. The cells were incubated with the inhibitors at the indicated concentrations for 24 h before cell lysis and luminescence measurement. Error bars represent ±SD across technical replicates (n = 2).

(F) Next-generation sequencing analysis of *eGFP* indicating the dose and time-dependent inhibition of SpCas9 by BRD0539 in U2OS.eGFP.PEST cells. Cells were nucleofected with either SpCas9 or preformed SpCas9:gRNA ribonucleoprotein complex targeting the *eGFP* gene and were incubated with BRD0539 at the indicated concentrations for 10 and 18 h before harvesting the genomic DNA. Error bars represent ±SD across technical replicates (n = 2) of two biological replicates.

(G) Cellular impermeability of the anti-CRISPR protein AcrIIA4 assessed by lack of SpCas9 inhibition in the eGFP-disruption assay when AcrIIA4 is incubated in the media. As a positive control for AcrIIA4 activity, the cells were nucleofected with SpCas9:gRNA:AcrIIA4 and incubated for 48 h before imaging. To assess cell permeability, the cells were nucleofected either with SpCas9 or SpCas9:gRNA ribonucleoprotein complex followed by incubation with AcrIIA4 in the media. Error bars represent ±SD across technical replicates (n = 4).

(H) Reversibility of BRD0539- or AcrIIA4-mediated inhibition of SpCas9 in U2OS.eGFP.PEST cells in the eGFP-disruption assay. Cells were nucleofected with either SpCas9 or a preformed SpCas9:gRNA ribonucleoprotein complex or the SpCas9:gRNA:AcrIIA4 ternary complex with an *eGFP* gene targeting guide and then were incubated with either DMSO or 15 μM of BRD0539 followed by a pulse-chase over 2–24 h before imaging. Error bars represent ±SD across technical replicates (n = 2) of two biological replicates.

(I) Inhibition of SpCas9 nuclease activity by BRD0539 in a DNA cleavage assay. SpCas9:gRNA (5 nM) was incubated with BRD0539 at the indicated concentrations for 30 min at room temperature followed by the addition of linear DNA substrate (2,783 bp, puc57) and incubated for an additional 30 min at 37°C. The results were visualized by 1% agarose gel with SYBR Gold staining and were quantified using ImageJ. Error bars represent ±SD across technical replicates (n = 2).

(J) Stability of the compounds in human plasma as determined by ultra-performance liquid chromatography-mass spectrometry (UPLC/MS) using the multiple reaction monitoring (MRM) method. Each compound (5 μM) was incubated with 50% human plasma in PBS for 5 h before being processed for analysis. Error bars represent ±SEM for technical replicates (n = 3).

See also Figure S3, Table S1, and Data S1.

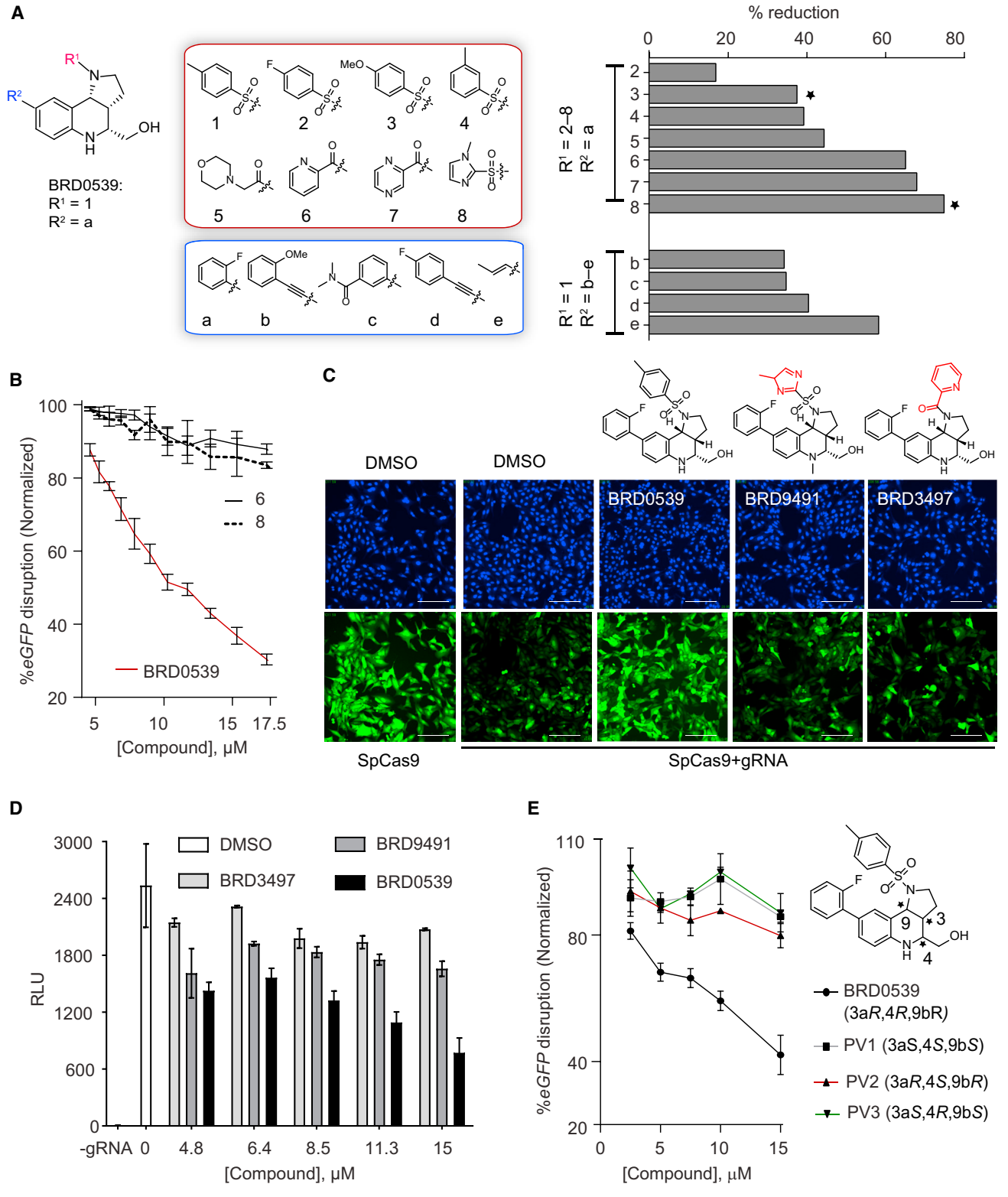

Figure 4. Structure-Activity Relationship

(A) Structure-activity relationship studies of BRD0539 in the eGFP-disruption assay in U2OS.eGFP.PEST cells. The top set of numbered functional groups represents variation at the 1-*N*-cap position (R^1), whereas those in the lettered bottom set represent variation at position 8 (R^2). The bar plot depicts the reduction

(legend continued on next page)

increasing numbers of PAM sequences (0–12 PAM, Figures 5D and S5A) or an increasing concentration of 8PAM DNA (Figures 5E and S5B). BRD0539 dose-dependently blocked the formation of the DNA-bound state in a dose-dependent fashion (Figures 5F and S5C). The SpCas9:gRNA exhibited a multiphasic melting signature that was altered upon the addition of DNA that contained PAM sequences. BRD0539 impaired the perturbation induced by the 4PAM DNA (Figure S5D; Supplementary Items 2 and 3 in https://doi.org/10.17632/jpxvnh3n2t.1). Finally, to confirm target engagement by BRD0539 in cells, we used the cellular thermal shift assay (CETSA), a cellular version of the DSF assay (Martinez Molina and Nordlund, 2016). Since SpCas9:DNA interactions increase the melting temperature of SpCas9, disrupting such interactions by BRD0539 should lower the melting temperature of SpCas9, and we do observe ~2.5°C lowering in cells treated with BRD0539 (Figures 5G and S5E; Supplementary Item 4 in https://doi.org/10.17632/jpxvnh3n2t.1). The interaction between BRD0539 and SpCas9 was further confirmed by pull-down studies in which biotinylated BRD0539 was able to pull down SpCas9 from WM793-SpCas9 cell lysate (Figures 5H and S5F), while no notable non-specific protein pull-down was observed (Supplementary Item 5 in https://doi.org/10.17632/jpxvnh3n2t.1). Finally, while BRD0539 was able to inhibit SpCas9 in the eGFP-disruption assay, BRD0539 was unable to inhibit FnCpf1, a structurally different CRISPR-associated nuclease, in the same assay, further highlighting the specificity of BRD0539 (Figure 5I).

Inhibition of the dCas9-Based Transcription Activation Complex

After optimizing the inhibition of the nuclease activity of the SpCas9:gRNA complex, we sought to optimize for inhibition of the transcriptional activation complex, which consists of dCas9:gRNA and transcription-activating SAM domains (Konermann et al., 2015) that are recruited by the gRNA. Our hit-triage workflow was similar to that for the nuclease activity and involved prioritizing compounds based on the absence of cytotoxicity and the presence of dose-dependent inhibition of transcriptional activation in cells. While the nuclease inhibitors identified above also blocked transcription (Figure S5G), BRD20322 and BRD0048 emerged as the most potent inhibitors of the transcription activation complex, showing a dose-dependent inhibition with an EC_{50} of 12.2 μM and 9 μM, with BRD20322 inhibiting 89% of the transcription at 20 μM (Figures 5J and S5H). None of the inhibitors altered the expression of the control genes.

DISCUSSION

We report a workflow for the rapid identification of small-molecule inhibitors of SpCas9 and demonstrate the utility of this workflow by identifying the first examples of small-molecule inhibitors of SpCas9. Our screening strategy involved disrupting DNA binding by SpCas9, followed by demonstrating activity in multiple mammalian cell lines using gene or protein delivery. Furthermore, we demonstrated inhibition of SpCas9 nuclease and transcription activation in assays with gain of signal (e.g., eGFP-disruption assay), loss of signal (e.g., HiBiT assay), various DNA repair pathways, and a myriad of readouts (e.g., fluorescence, luminescence, next-generation sequencing [NGS], qPCR). Thus, these inhibitors are effective against both wild-type and engineered SpCas9 in mammalian cells with multiple delivery modes, including delivery of the ribonucleoprotein complex. Our inhibitor identification methodology is rapid and cost effective and required testing only ~15,000 compounds to identify potent SpCas9 inhibitors. We envision that the availability of high-throughput assays and a screening workflow will propel the rapid discovery of highly potent inhibitors, not only for SpCas9 but also for next-generation CRISPR-associated nucleases. Finally, the small-molecule inhibitors complement protein-based anti-CRISPRs in that they are cell permeable, reversible, stable in human plasma, and resistant to proteases.

Multiple lines of evidence point to the specific nature of interactions between the inhibitors and the SpCas9:gRNA complex. Small perturbations to the structure or even the stereochemistry of BRD0539 causes loss of inhibitory activity, and FnCpf1 remains uninhibited by BRD0539. Furthermore, the subtle structural variation between inhibitors that block the SpCas9:gRNA complex from those that inhibit the dCas9:gRNA:SAM complex for transcription activation also points to specific interactions. The ability of identified inhibitor BRD0539 to block the formation of the DNA-bound state indicates that the reported inhibitors could either operate by directly competing with the NGG PAM or bind to an allosteric site. Identifying the binding pocket of the inhibitors via structural studies will be key for mechanistic understanding of the aforementioned observations as well as

in activity of different structural analogs with respect to that of BRD0539. Asterisk-labeled compounds have a methyl group at the 4-*N* position, while the others have a proton. The data are an average of two biological replicates.

(B) Dose-dependent inhibition of SpCas9 by BRD0539, BRD3497, and BRD9419 in U2OS.eGFP.PEST cells. The inhibitors were tested from 2.8 to 17.3 μM. U2OS.eGFP.PEST cells were nucleofected with either SpCas9 or preformed SpCas9:gRNA ribonucleoprotein complex and were incubated with the compounds at the indicated concentrations for 24 h before imaging. Error bars represent ±SD across technical replicates (n = 3).

(C) Representative images of the eGFP-disruption assay. U2OS.eGFP.PEST cells were nucleofected with either SpCas9 alone (untreated) or preformed SpCas9:gRNA ribonucleoprotein complex and were treated with either vehicle alone or the indicated compounds at 15 μM for 24 h. The top and bottom panels represent DAPI and GFP channels, respectively.

(D) Dose-dependent inhibition of SpCas9 by BRD0539, BRD3497, and BRD9419 in the HiBiT assay. Inhibitors were tested from 4.8 to 15 μM. U2OS.eGFP.PEST cells were nucleofected with SpCas9- and gRNA-expressing plasmids along with ssODN containing the HiBiT tag. The cells were incubated with compounds at the indicated concentrations for 24 h before cell lysis and luminescence measurements. Error bars represent ±SD across technical replicates (n = 2).

(E) Chemical structures of BRD0539 stereoisomers and their dose-dependent inhibition of SpCas9 in U2OS.eGFP.PEST cells. Inhibitors were tested from 4.6–17.5 μM. Cells were nucleofected with either SpCas9 or preformed SpCas9:gRNA ribonucleoprotein complex and were incubated with the compounds at the indicated concentration for 24 h before imaging. Error bars represent ±SD across technical replicates (n = 3).

See also Figure S4, Table S1, and Data S1.

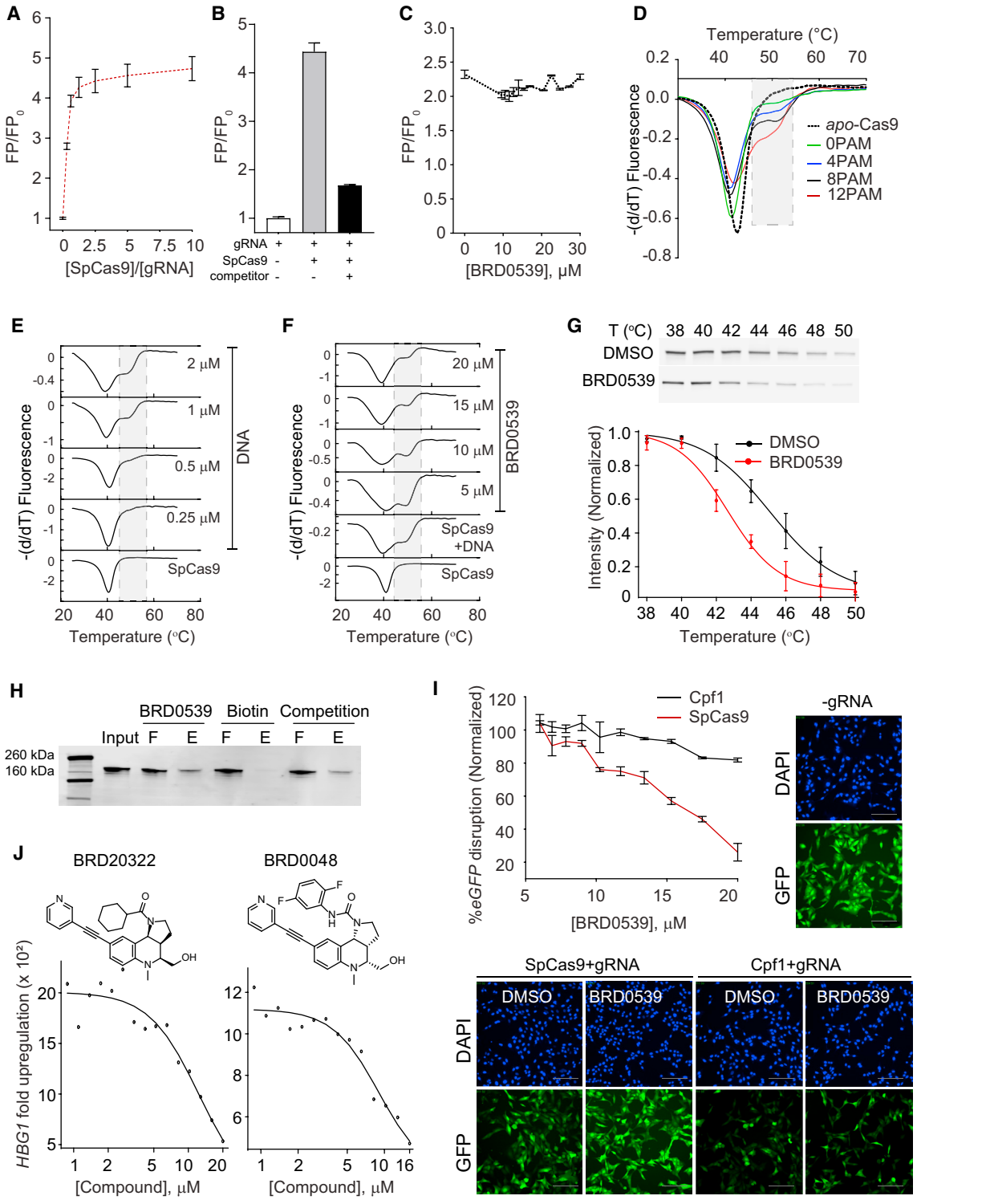

Figure 5. Mechanism of Action and Inhibition of dCas9-Based Transcriptional Upregulation

(A) FP assay for detecting SpCas9-gRNA binding. A FITC-labeled crRNA:tracrRNA (25 nM) was titrated with an increasing amount of SpCas9 (7.5–250 nM). Error bars represent ±SD across technical replicates (n = 3).

(B) Competition experiment demonstrating sequence-specific gRNA-SpCas9 binding. An unlabeled crRNA:tracrRNA (25 nM) was pre-incubated with SpCas9 (25 nM) for 10 min before the addition of FITC-crRNA:tracrRNA (25 nM). Error bars represent ±SD across technical replicates (n = 3).

(legend continued on next page)

potency improvement of the inhibitors. Mechanism-of-action studies involving single-molecule biophysics experiments to examine the effects of the inhibitor on the conformational change of SpCas9 during the catalytic cycle will also provide valuable insight and may explain the molecular mechanism of disruption of DNA binding as suggested by DSF studies. We note that our DSF studies confirm the presence of a flexible conformation of *apo*-SpCas9 that shows a preference for DNA containing PAM sequences (Figure 5D). *Apo*-SpCas9 binds to DNA with an affinity of 25 nM (Sternberg et al., 2014), and high-speed atomic force microscopy studies suggest the presence of a flexible conformation in solution (Shibata et al., 2017) as opposed to the closed conformation observed in crystal structures.

Identifying small-molecule inhibitors of nuclease activity presents similar assay development challenges as we encountered for PAM binding. Our future studies will involve the identification of nuclease inhibitors and an exploration of possible synergies between the two classes of inhibitors. Although our inhibitors are nontoxic to mammalian cells and do not alter transcription and translation of housekeeping genes, it remains to be determined whether these inhibitors or the anti-CRISPR proteins interact with other targets in mammalian cells. Finally, in many applications, degradation of SpCas9 may be required. For example, a recent study has pointed to the existence of antibodies against SpCas9 in humans (Charlesworth et al., 2018), and the SpCas9-specific immune response is construed as a bottleneck in the development of therapeutic applications of SpCas9. Reducing the half-life of SpCas9 may reduce the severity of the immune response. Proteolysis-targeting chimeras (PROTACs) are heterobifunctional small molecules containing a target-protein binder and a ubiquitin-ligase binder joined by a linker (Lai and Crews, 2017). A PROTAC formed by joining our inhibitor to the ubiquitin-ligase binder should recruit ubiquitin ligase to SpCas9, promoting ubiquitination and proteasomal degradation of SpCas9. Furthermore, PROTACs are catalytic and may require a lower dose as they operate by "event-driven pharmacology" as opposed to inhibitors that are stoichiometric and operate by "occupancy-driven pharmacology." Our future efforts will involve the identification of inhibitors for next-generation CRISPR systems and understanding their mode of inhibition as well as the application of such inhibitors. The timely and partial inhibition (~50%) of SpCas9 reduced off-target editing for several genes, including a 5-fold reduction for β-globin (*HBB*)-targeting gRNA that is of therapeutic interest for sickle cell disease (Shin et al., 2017). Partial inhibition of SpCas9 by BRD0539 together with its cellular permeability, reversibility, and plasma stability should afford a facile method for reducing the off-target activity of SpCas9. Together, our studies point to the utility of invocation of chemical biology-based approaches for genome editing and functional genomics studies using CRISPR-based systems.

STAR★METHODS

Detailed methods are provided in the online version of this paper and include the following:

- KEY RESOURCES TABLE
- CONTACT FOR REAGENT AND RESOURCE SHARING
- EXPERIMENTAL MODEL AND SUBJECT DETAILS
  - *Escherichia coli* Rosetta (DE3)
  - *Escherichia coli* BL21 (DE3)
  - Cell culture
- METHOD DETAILS

(C) FP assay for determining the effect of BRD0539 in the SpCas9-FITC-crRNA:tracrRNA binding. SpCas9 (25 nM) was incubated with the indicated amount of BRD0539 (10–30 μM) for 15 min followed by the addition of FITC-crRNA:tracrRNA (25 nM), which was incubated for 30 min before measuring the FP signal. Error bars represent ±SD across technical replicates (n = 3).

(D) Differential scanning fluorimetry studies of the *apo*-SpCas9 interaction with DNA. SpCas9 (1 μM) was incubated with DNA (2 μM) bearing an increasing number of PAM sequences (0–12 PAM). Data are for one of the three biological replicates.

(E) Differential scanning fluorimetry showing the formation of a more stable SpCas9 complex (shaded region) upon binding with increasing concentrations (0.25, 0.5, 1, and 2 μM) of 8PAM DNA. Error bars represent ±SD across technical replicates (n = 2).

(F) Differential scanning fluorimetry depicting the destabilization of SpCas9:8PAM DNA (1 μM:2 μM) complexes (shaded region) upon incubation with increasing concentrations (5, 10, 15, and 20 μM) of BRD0539. Error bars represent ±SD across technical replicates (n = 2).

(G) Cellular thermal shift assay (CETSA) for SpCas9 in WM793 melanoma cells in the absence or presence of BRD0539. WM793 cells stably expressing SpCas9 were incubated with 15 μM BRD0539 for 24 h before performing CETSA and were analyzed by western blot. The top panel is the immunoblot representation of the thermal stability of SpCas9 in WM793 cells treated with either vehicle or BRD0539. The original immunoblot is in the Supplementary Item 4 (https://doi.org/10.17632/jpxvnh3n2t.1). The bottom panel is the quantified thermal stability plot for SpCas9. Error bars represent ±SD across biological replicates (n = 4).

(H) *In vitro* pull-down assay of SpCas9 by the BRD0539-biotin conjugate from WM793-SpCas9 cell lysate. Streptavidin magnetic beads pre-loaded with either BRD0539-biotin or biotin-azide were incubated with WM793-SpCas9 cell lysate for 12 h before processing the samples for western blotting. BRD0539 (20 μM) was used as a competitor. F and E represent the flow-through and eluent, respectively.

(I) Dose-dependent inhibition study of BRD0539 (6–20 μM) against SpCas9 or FnCpf1 in U2OS.eGFP.PEST cells. Cells were nucleofected with SpCas9 or FnCpf1 plasmids and their corresponding gRNA-expressing plasmids and were incubated with the inhibitor at the indicated concentration for 30 h before imaging and analysis. Error bars represent ±SD across technical replicates (n = 4). Representative images of the eGFP-disruption assay for SpCas9 and FnCpf1 in U2OS.eGFP.PEST cells. Cells were nucleofected with either SpCas9 plasmid alone (–gRNA) or either the SpCas9 or FnCpf1 plasmids with their corresponding gRNA-expressing plasmids containing the *eGFP* gene target and were incubated with the inhibitor (15 μM) for 30 h before imaging. The top and bottom panels represent the DAPI and GFP channels, respectively.

(J) Chemical structures of BRD20322 and BRD0048 and their dose-dependent inhibition of dCas9-based transcriptional upregulation of the *HBG1* gene in HEK293FT cells. Cells were transfected with dSpCas9 and MS2.p65.HSF1.GFP plasmids along with either *RFP* or *HBG1* gRNA plasmids and were incubated in the presence of the small molecules at the indicated concentrations before processing for RT-qPCR. The experiments were performed in three biological replicates, and each biological replicate was processed in eight technical replicates. The data represent the mean ± SEM for technical replicates. *$p \leq 0.0001$ for both small molecules at 15 μM and DMSO (unpaired t test, two-tailed).

See also Figure S5, Table S1, and Data S1.

SUPPLEMENTAL INFORMATION

Supplemental Information can be found online at https://doi.org/10.1016/j.cell.2019.04.009.

ACKNOWLEDGMENTS

This work was supported by the Burroughs Wellcome Fund (Career Award at the Scientific Interface to A.C.), DARPA (Brdi N66001-17-2-4055 to A.C.; HR0011-17-2-0049 to D.R.L.), NIH (R21AI126239 to A.C.; RM1HG009490 and R35 GM118062 to D.R.L.), and Army Research Office award W911NF1610586 (to A.C.). We thank Prof. M.D. Shoulders, Dr. K.J. Cox, and Dr. D. Manna for contributive discussions; Prof. J. Keith Joung for providing U2OS.eGFP.PEST cells; and H. Li for providing WM793-SpCas9 cells. D.R.L. and L.A.M. are investigators of the Howard Hughes Medical Institute.

AUTHOR CONTRIBUTIONS

A.C. conceptualized the project and Cas9 assays. B. Maji developed Cas9 assays and performed small-molecule screening, activity optimization, and SAR studies. B. Maji, V.D., B.K.W., and A.C. analyzed the screening data. M.L., M.S., and P.W. performed chemical synthesis. B. Maji, S.A.G., M.L., M.S., P.W., R.H., B. Mok, S.U.S., D.L., B.P., A.V., and M.F.M. performed validation experiments and analyzed data with L.A.M., D.R.L., P.A.C., B.K.W., or A.C. The manuscript was written by B. Maji, S.A.G., M.L., M.S., P.W., B.K.W., and A.C. and was edited by all the authors.

DECLARATION OF INTERESTS

Broad Institute has filed a patent application including work described herein. L.A.M. is a cofounder and Scientific Advisory Board member of Intellia Therapeutics and a co-founder of Eligo Biosciences. D.R.L. is a co-founder and consultant of Editas Medicine, Pairwise Plants, and Beam Therapeutics, companies that use genome editing.

Received: December 14, 2017
Revised: September 17, 2018
Accepted: April 3, 2019
Published: May 2, 2019

SUPPORTING CITATIONS

The following references appear in the Supplemental Information: Tan and Jacobsen (2007); Xu et al. (2014).

REFERENCES

Champer, J., Buchman, A., and Akbari, O.S. (2016). Cheating evolution: engineering gene drives to manipulate the fate of wild populations. Nat. Rev. Genet. *17*, 146–159.

Charlesworth, C.T., Deshpande, P.S., Dever, D.P., Dejene, B., Gomez-Ospina, N., Mantri, S., Pavel-Dinu, M., Camarena, J., Weinberg, K.I., and Porteus, M.H. (2018). Identification of pre-existing adaptive immunity to Cas9 proteins in humans. bioRxiv. https://doi.org/10.1101/243345.

Chen, J.S., and Doudna, J.A. (2017). The chemistry of Cas9 and its CRISPR colleagues. Nat. Rev. Chem. *1*, 0078.

Comer, E., Duvall, J.R., and duPont Lee, M., 4th. (2014). Utilizing diversity-oriented synthesis in antimicrobial drug discovery. Future Med. Chem. *6*, 1927–1942.

Comer, E., Munoz, B., Beaudoin, J.A., Le Quement, S.T., Scherer, C., Duvall, J., Kato, N., Maetani, M., and Braibant, B. (2015). Compounds for the treatment of malaria. WIPO patent WO2015002755, filed June 20, 2014, and granted January 8, 2015.

Cox, D.B.T., Platt, R.J., and Zhang, F. (2015). Therapeutic genome editing: prospects and challenges. Nat. Med. *21*, 121–131.

Cox, K.J., Subramanian, H.K.K., Samaniego, C.C., Franco, E., and Choudhary, A. (2019). A universal method for sensitive and cell-free detection of CRISPR-associated nucleases. Chem. Sci. (Camb.).

Di, L., Kerns, E.H., Hong, Y., and Chen, H. (2005). Development and application of high throughput plasma stability assay for drug discovery. Int. J. Pharm. *297*, 110–119.

Esvelt, K.M., Smidler, A.L., Catteruccia, F., and Church, G.M. (2014). Concerning RNA-guided gene drives for the alteration of wild populations. eLife *3*, e03401.

Fellmann, C., Gowen, B.G., Lin, P.C., Doudna, J.A., and Corn, J.E. (2017). Cornerstones of CRISPR-Cas in drug discovery and therapy. Nat. Rev. Drug Discov. *16*, 89–100.

Fu, Y., Foden, J.A., Khayter, C., Maeder, M.L., Reyon, D., Joung, J.K., and Sander, J.D. (2013). High-frequency off-target mutagenesis induced by CRISPR-Cas nucleases in human cells. Nat. Biotechnol. *31*, 822–826.

Gangopadhyay, S.A., Cox, K.J., Manna, D., Lim, D., Maji, B., Zhou, Q., and Choudhary, A. (2019). Precision Control of CRISPR-Cas9 Using Small Molecules and Light. Biochemistry. Biochemistry *29*, 234–244.

Gantz, V.M., and Bier, E. (2016). The dawn of active genetics. BioEssays *38*, 50–63.

Gerard, B., O'Shea, M.W., Donckele, E., Kesavan, S., Akella, L.B., Xu, H., Jacobsen, E.N., and Marcaurelle, L.A. (2012). Application of a catalytic asymmetric Povarov reaction using chiral ureas to the synthesis of a tetrahydroquinoline library. ACS Comb. Sci. *14*, 621–630.

Gerry, C.J., and Schreiber, S.L. (2018). Chemical probes and drug leads from advances in synthetic planning and methodology. Nat. Rev. Drug Discov. *17*, 333–352.

Hynes, A.P., Rousseau, G.M., Lemay, M.L., Horvath, P., Romero, D.A., Fremaux, C., and Moineau, S. (2017). An anti-CRISPR from a virulent streptococcal phage inhibits Streptococcus pyogenes Cas9. Nat. Microbiol. *2*, 1374–1380.

Jinek, M., Chylinski, K., Fonfara, I., Hauer, M., Doudna, J.A., and Charpentier, E. (2012). A programmable dual-RNA-guided DNA endonuclease in adaptive bacterial immunity. Science *337*, 816–21.

Kleinstiver, B.P., Prew, M.S., Tsai, S.Q., Nguyen, N.T., Topkar, V.V., Zheng, Z., and Joung, J.K. (2015a). Broadening the targeting range of Staphylococcus aureus CRISPR-Cas9 by modifying PAM recognition. Nat. Biotechnol. *33*, 1293–1298.

Kleinstiver, B.P., Prew, M.S., Tsai, S.Q., Topkar, V.V., Nguyen, N.T., Zheng, Z., Gonzales, A.P., Li, Z., Peterson, R.T., Yeh, J.R., et al. (2015b). Engineered CRISPR-Cas9 nucleases with altered PAM specificities. Nature *523*, 481–485.

Koehler, A.N. (2010). A complex task? Direct modulation of transcription factors with small molecules. Curr. Opin. Chem. Biol. *14*, 331–340.

Komor, A.C., Kim, Y.B., Packer, M.S., Zuris, J.A., and Liu, D.R. (2016). Programmable editing of a target base in genomic DNA without double-stranded DNA cleavage. Nature *533*, 420–424.

Komor, A.C., Badran, A.H., and Liu, D.R. (2017). CRISPR-based technologies for the manipulation of eukaryotic genomes. Cell *168*, 20–36.

Konermann, S., Brigham, M.D., Trevino, A.E., Joung, J., Abudayyeh, O.O., Barcena, C., Hsu, P.D., Habib, N., Gootenberg, J.S., Nishimasu, H., et al. (2015). Genome-scale transcriptional activation by an engineered CRISPR-Cas9 complex. Nature *517*, 583–588.

Lai, A.C., and Crews, C.M. (2017). Induced protein degradation: an emerging drug discovery paradigm. Nat. Rev. Drug Discov. *16*, 101–114.

Maji, B., Moore, C.L., Zetsche, B., Volz, S.E., Zhang, F., Shoulders, M.D., and Choudhary, A. (2017). Multidimensional chemical control of CRISPR-Cas9. Nat. Chem. Biol. *13*, 9–11.

Martinez Molina, D., and Nordlund, P. (2016). The Cellular Thermal Shift Assay: A novel biophysical assay for in situ drug target engagement and mechanistic biomarker studies. Annu. Rev. Pharmacol. Toxicol. *56*, 141–161.

Moore, R., Spinhirne, A., Lai, M.J., Preisser, S., Li, Y., Kang, T., and Bleris, L. (2015). CRISPR-based self-cleaving mechanism for controllable gene delivery in human cells. Nucleic Acids Res. *43*, 1297–1303.

Neve, R.L., Neve, K.A., Nestler, E.J., and Carlezon, W.A., Jr. (2005). Use of herpes virus amplicon vectors to study brain disorders. Biotechniques *39*, 381–391.

Nguyen, D.P., Miyaoka, Y., Gilbert, L.A., Mayerl, S.J., Lee, B.H., Weissman, J.S., Conklin, B.R., and Wells, J.A. (2016). Ligand-binding domains of nuclear receptors facilitate tight control of split CRISPR activity. Nat. Commun. *7*, 12009.

Nishimasu, H., Ran, F.A., Hsu, P.D., Konermann, S., Shehata, S.I., Dohmae, N., Ishitani, R., Zhang, F., and Nureki, O. (2014). Crystal structure of Cas9 in complex with guide RNA and target DNA. Cell *156*, 935–949.

Nuñez, J.K., Harrington, L.B., and Doudna, J.A. (2016). Chemical and biophysical modulation of Cas9 for tunable genome engineering. ACS Chem. Biol. *11*, 681–688.

Pattanayak, V., Lin, S., Guilinger, J.P., Ma, E., Doudna, J.A., and Liu, D.R. (2013). High-throughput profiling of off-target DNA cleavage reveals RNA-programmed Cas9 nuclease specificity. Nat. Biotechnol. *31*, 839–843.

Pawluk, A., Amrani, N., Zhang, Y., Garcia, B., Hidalgo-Reyes, Y., Lee, J., Edraki, A., Shah, M., Sontheimer, E.J., Maxwell, K.L., et al. (2016a). Naturally occurring off-switches for CRISPR-Cas9. Cell *167*, 1829–1838.

Pawluk, A., Staals, R.H., Taylor, C., Watson, B.N., Saha, S., Fineran, P.C., Maxwell, K.L., and Davidson, A.R. (2016b). Inactivation of CRISPR-Cas systems by anti-CRISPR proteins in diverse bacterial species. Nat. Microbiol. *1*, 16085.

Rauch, B.J., Silvis, M.R., Hultquist, J.F., Waters, C.S., McGregor, M.J., Krogan, N.J., and Bondy-Denomy, J. (2017). Inhibition of CRISPR-Cas9 with bacteriophage proteins. Cell *168*, 150–158.

Rees, H.A., Komor, A.C., Yeh, W.H., Caetano-Lopes, J., Warman, M., Edge, A.S.B., and Liu, D.R. (2017). Improving the DNA specificity and applicability of base editing through protein engineering and protein delivery. Nat. Commun. *8*, 15790.

Richardson, C.D., Ray, G.J., DeWitt, M.A., Curie, G.L., and Corn, J.E. (2016). Enhancing homology-directed genome editing by catalytically active and inactive CRISPR-Cas9 using asymmetric donor DNA. Nat. Biotechnol. *34*, 339–344.

Schreiber, S.L. (2000). Target-oriented and diversity-oriented organic synthesis in drug discovery. Science *287*, 1964–1969.

Schwinn, M.K., Machleidt, T., Zimmerman, K., Eggers, C.T., Dixon, A.S., Hurst, R., Hall, M.P., Encell, L.P., Binkowski, B.F., and Wood, K.V. (2018). CRISPR-mediated tagging of endogenous proteins with a luminescent peptide. ACS Chem. Biol. *13*, 467–474.

Shibata, M., Nishimasu, H., Kodera, N., Hirano, S., Ando, T., Uchihashi, T., and Nureki, O. (2017). Real-space and real-time dynamics of CRISPR-Cas9 visualized by high-speed atomic force microscopy. Nat. Commun. *8*, 1430.

Shin, J., Jiang, F., Liu, J.-J., Bray, N.L., Rauch, B.J., Baik, S.H., Nogales, E., Bondy-Denomy, J., Corn, J.E., and Doudna, J.A. (2017). Disabling Cas9 by an anti-CRISPR DNA mimic. Sci. Adv. *3*, e1701620.

Sternberg, S.H., Redding, S., Jinek, M., Greene, E.C., and Doudna, J.A. (2014). DNA interrogation by the CRISPR RNA-guided endonuclease Cas9. Nature *507*, 62–67.

Tan, K.L., and Jacobsen, E.N. (2007). Indium-mediated asymmetric allylation of acylhydrazones using a chiral urea catalyst. Angew. Chem. Int. Ed. Engl. *46*, 1315–1317.

Tu, Z., Yang, W., Yan, S., Yin, A., Gao, J., Liu, X., Zheng, Y., Zheng, J., Li, Z., Yang, S., et al. (2017). Promoting Cas9 degradation reduces mosaic mutations in non-human primate embryos. Sci. Rep. *7*, 42081.

Wang, H., Yang, H., Shivalila, C.S., Dawlaty, M.M., Cheng, A.W., Zhang, F., and Jaenisch, R. (2013). One-step generation of mice carrying mutations in multiple genes by CRISPR/Cas-mediated genome engineering. Cell *153*, 910–918.

Wang, H., La Russa, M., and Qi, L.S. (2016). CRISPR/Cas9 in genome editing and beyond. Annu. Rev. Biochem. *85*, 227–264.

Wawer, M.J., Li, K., Gustafsdottir, S.M., Ljosa, V., Bodycombe, N.E., Marton, M.A., Sokolnicki, K.L., Bray, M.A., Kemp, M.M., Winchester, E., et al. (2014). Toward performance-diverse small-molecule libraries for cell-based phenotypic screening using multiplexed high-dimensional profiling. Proc. Natl. Acad. Sci. USA *111*, 10911–10916.

Wegrzyn, R.D., Lee, A.H., Jenkins, A.L., Stoddard, C.D., and Cheever, A.E. (2017). Genome editing: insights from chemical biology to support safe and transformative therapeutic applications. ACS Chem. Biol. https://doi.org/10.1021/acschembio.1027b00689.

Weiss, W.A., Taylor, S.S., and Shokat, K.M. (2007). Recognizing and exploiting differences between RNAi and small-molecule inhibitors. Nat. Chem. Biol. *3*, 739–744.

Xu, H., Zhang, H., and Jacobsen, E.N. (2014). Chiral sulfinamidourea and strong Brønsted acid-cocatalyzed enantioselective Povarov reaction to access tetrahydroquinolines. Nat. Protoc. *9*, 1860–1866.

Yen, S.-T., Zhang, M., Deng, J.M., Usman, S.J., Smith, C.N., Parker-Thornburg, J., Swinton, P.G., Martin, J.F., and Behringer, R.R. (2014). Somatic mosaicism and allele complexity induced by CRISPR/Cas9 RNA injections in mouse zygotes. Dev. Biol. *393*, 3–9.

Zhang, J.H., Chung, T.D., and Oldenburg, K.R. (1999). A simple statistical parameter for use in evaluation and validation of high throughput screening assays. J. Biomol. Screen. *4*, 67–73.

STAR★METHODS

KEY RESOURCES TABLE

REAGENT or RESOURCE	SOURCE	IDENTIFIER
Antibodies		
Anti-GFP antibody	Cell Signaling	Cat# 2956; RRID:AB_1196615
Anti-actin	Sigma	Cat# A2228; RRID:AB_476697
Bacterial and Virus Strains		
Escherichia coli DH5 alpha cells	NEB	Cat# C2987I
Escherichia coli Rosetta (DE3)	NEB	Cat# C25271
Chemicals, Peptides, and Recombinant Proteins		
HCS NuclearMask	Thermo Fisher Scientific	Cat# H10325
T4 PNK	NEB	Cat# M0201S
T4 ligase	NEB	Cat# M0202
BsmBI	NEB	Cat# R0580S
Tobacco Etch Virus (TEV) protease	SIGMA-ALDRICH	Cat# T4455-10KU
Phusion Hot Start II DNA polymerase	New England Biolabs	Cat# F-549
Fetal Bovine Serum (For mammalian cell culture)	Sigma Aldrich	Cat# F4135
Penicillin-Streptomycin (For mammalian cell culture)	Sigma Aldrich	Cat# P4333
poly-D-lysine	Sigma Aldrich	Cat# P6407
Lipofectamine 2000	Thermo Fisher	Cat# 11668019
Q5 High-Fidelity DNA Polymerase	NEB	Cat# M0491S
DMEM (Medium for mammalian cell culture)	Thermo Fisher Scientific	Cat# 10564-011
SYPRO Orange	Invitrogen	Cat# S6650
XPhos-Pd-G2	Sigma Aldrich	Cat# 741825
XPhos-Pd-G3	Sigma Aldrich	Cat# 763381
1,4-diazabicyclo[2.2.2]octane	Sigma Aldrich	Cat# D27802
4-pyridinecarboxyaldehyde	Sigma Aldrich	Cat# P62402
Sodium triacetoxyborohydride	Oakwood Chemical	Cat# 044864
2,6-Dimethylpyridine	Oakwood Chemical	Cat# 092726
PyBop	Combi-Blocks	Cat# ST-8688
Biotin-PEG3-acid	Broadpharm	Cat# BP-20699
3-Methoxyphenylboronic acid	Sigma Aldrich	Cat# 441686
2-Fluorophenylboronic acid	Sigma Aldrich	Cat# 445223
P-Toluenesulfonylchloride	Oakwood Chemical	Cat# BR1703
3,3-Dimethylbutyryl chloride	Sigma Aldrich	Cat# B88802
3-Ethynylpyridine	Oakwood Chemical	Cat# 080053
Cyclohexanecarbonyl chloride	Oakwood Chemical	Cat# 099402
2,5-Difluorophenyl isocyanate	Oakwood Chemical	Cat# 024269
Deposited Data		
eGFP-disruption assay	This paper	Mendeley Data (video files 1-8) https://doi.org/10.17632/jpxvnh3n2t.1
Cytotoxicity	This paper	Mendeley Data (Supplementary item 1) https://doi.org/10.17632/jpxvnh3n2t.1
DSF data	This paper	Mendeley Data (Supplementary item 2-3) https://doi.org/10.17632/jpxvnh3n2t.1
Immunoblots	This paper	Mendeley Data (Supplementary item 4) https://doi.org/10.17632/jpxvnh3n2t.1

(*Continued on next page*)

Continued

REAGENT or RESOURCE	SOURCE	IDENTIFIER
Pulldown data	This paper	Mendeley Data (Supplementary item 5) https://doi.org/10.17632/jpxvnh3n2t.1
NGS data	This paper	Mendeley Data https://doi.org/10.17632/jpxvnh3n2t.1
Chemical characterizations	This paper	Data S1,
Experimental Models: Cell Lines		
Human: HEK293T	ATCC	Cat# CRL-3216
Human: HEK293FT	Feng Zhang lab	NA
Human: U2OS.eGFP.PEST	Keith Joung lab	NA
Bone marrow stroma	Stuart Schreiber lab	NA
WM793-SpCas9	Stuart Schreiber lab	NA
Oligonucleotides		
FITC labeled oligos	IDT	Table S1
Biotin oligos	IDT	Table S1
Primers	IDT and Eton Bio.	Table S1
Recombinant DNA		
pMJ806	Jinek et al., 2012	Addgene Cat# 39312
JDS246	Fu et al., 2013	Addgene Cat# 43861
pFYF1320 EGFP SiteCat# 1	Fu et al., 2013	Addgene Cat# 47511
BPK1520	Kleinstiver et al., 2015b	Addgene Cat# 65777
MS2-P65-HSF1	Maji et al., 2017	NA
dSpCas9	Feng Zhang lab	NA
Critical Commercial Assays		
MEGAClear Transcription Clean Up Kit RNA purification	Thermo Fisher	Cat# AM1908
High Precision Streptavidin (SAX) Biosensors	ForteBio	Cat# 18-5117
SE. Cell Line 4D-Nucleofector X Kit	Lonza	Cat# V4XC-1032
Qubit dsDNA HS Kit	Thermo Fisher	Cat# Q32851
Nano-Glo HiBiT Lytic Reagent	Promega	Cat# N3030
TaqMan probes	Life Technologies	Cat# 4331182
QuickExtract	Epicenter	Cat# QE09050
Surveyor Mutation Detection Kits	IDT	Cat# 706020
MiSeq Reagent Kit v2 300	Illumina	Cat# MS-102-2002
Streptavidin magnetic beads	Thermo Fisher Scientific	Cat# 88816
RevertAid RT Reverse Transcription Kit	Thermo Fischer Scientific	Cat# K1691
Ni-NTA agarose resin	Thermo Fisher Scientific	Cat# R90110
QIAamp DNA Mini Kit	QIAGEN	Cat# 51306
Software and Algorithms		
GraphPad Prism	GraphPad Prism Software	https://www.graphpad.com/scientific-software/prism/
Spotfire	Tibco	https://www.tibco.com/products/tibco-spotfire
MetaXpress	Molecular Device	https://www.moleculardevices.com/products/cellular-imaging-systems/acquisition-and-analysis-software/metaxpress#gref
MATLAB	MathWorks	https://in.mathworks.com/
MATLAB Script	Komor et al., 2017	N/A

CONTACT FOR REAGENT AND RESOURCE SHARING

Further information and requests for resources and reagents should be directed to and will be fulfilled by the Lead Contact, Amit Choudhary (achoudhary@bwh.harvard.edu).

EXPERIMENTAL MODEL AND SUBJECT DETAILS

Escherichia coli Rosetta (DE3)

E. coli Rosetta (DE3) cells were used for protein expression for *in vitro* and cellular studies. Cells were grown at 37°C (unless otherwise indicated) in Terrific Broth (TB) medium supplemented with 25 mg/mL kanamycin for plasmid maintenance.

Escherichia coli BL21 (DE3)

This strain was used for recombinant anti-CRISPR protein expression for cellular studies. Cells were grown at 37°C (unless otherwise indicated) in LB medium supplemented with 100 mg/mL ampicillin for plasmid maintenance.

Cell culture

All cells were cultured at 37°C in a humidified 5% CO_2 atmosphere. HEK293T cells (ATCC, female) used in transcriptional activation, NHEJ, and mCherry-disruption assays were cultured in Dulbecco's modified Eagle's medium (DMEM, Life Technologies) supplemented with 10% fetal bovine serum (FBS, Sigma Aldrich) and 1 × penicillin/streptomycin/glutamax (Life Technologies). U2OS.eGFP.PEST cells (human, female) stably integrated with an *eGFP.PEST* fusion gene were maintained in DMEM supplemented with 10% FBS, 1 × penicillin/streptomycin/glutamax, and 400 μg/mL G418 (selection antibiotic). WM793 cells (human, male) were cultured in RPMI1640 (Life Technologies) media supplemented with 10% FBS and 1 × penicillin/streptomycin/glutamax. Human islets (female) were maintained in CMRL 1066 (Life Technologies) containing 10% FBS, 1 × penicillin/streptomycin/glutamax, and 1 mM sodium pyruvate and were cultivated at 37°C with 5% CO_2 in a humidified atmosphere. Human bone marrow-derived mesenchymal stem cells (hMSC, female) were cultured in DMEM supplemented with 10% FBS and 1 × penicillin/streptomycin/glutamax. Cells were continuously maintained at < 90% confluency. All cell lines were sourced commercially or were functionally validated. Cells were periodically tested for mycoplasma contamination using the MycoAlert PLUS Mycoplasma Detection Kit (Lonza).

METHOD DETAILS

SpCas9 expression and purification

SpCas9 was expressed and purified following a previously reported protocol (Pattanayak et al., 2013). Rosetta (DE3)-competent *E. coli* cells were transformed with plasmids encoding the bacterial-codon-optimized SpCas9 with a His6-MBP-TEV-N-terminal purification tag. A single colony was grown overnight in LB broth containing 25 μg/ml of kanamycin at 37°C. The cells were diluted 1:100 into 1 L of the same media and grown at 37°C until the OD600 = 0.6–0.7. The cultures were incubated at 18°C for 30 min, and protein expression was induced with 0.2 mM of isopropyl-β-D-1-thiogalactopyranoside (GoldBio). Expression was sustained for 16–18 h with shaking at 18°C. The subsequent purification steps were carried out at 4°C. Cells were collected by centrifugation and resuspended in cell-collection buffer (10 mM Tris-HCl, pH 8.0, 1 M KCl, 20% glycerol, 1 mM tris[2- carboxyethyl]phosphine [TCEP; GoldBio], and 0.4 mM phenylmethane sulfonyl fluoride [Sigma-Aldrich]. Cells were lysed by sonication (10 min total, 30 s on, 30 s off), and the lysate was cleared by centrifugation at 18,000 × g (60 min).

The cleared lysate was incubated with His-Pur nickel-nitriloacetic acid (nickel-NTA) resin with rotation at 4°C for 90 min. The resin was washed twice with 15 column volumes of cell-collection buffer before the bound protein was eluted with elution buffer (10 mM Tris-HCl, pH 7.4, 0.15 M KCl, 20% glycerol, 1 mM TCEP, 250 mM imidazole). Protein-containing fractions were concentrated using Amicon ultra centrifugal filter with a 100 kDa cutoff (Millipore) centrifuged at 3,000 × g, and the concentrated solution was dialyzed for 12 h in Tris-HCl buffer (10 mM Tris-HCl, pH 7.4, 0.15 M KCl, 20% glycerol, 1 mM TCEP) and incubated with ProTEV Plus (Promega) for an additional 24 h. The crude protein solution was passed through a Nickel-NTA column to remove the uncleaved substrate. The resulting protein fraction was further purified on a 5 mL HiTrap SP FF (GE Healthcare) cation exchange column with an elution buffer containing a linear KCl gradient from 0.1 M to 1 M over five column volumes using an Akta Pure FPLC. The protein-containing fractions were concentrated using Amicon ultra centrifugal filter with a 100 kDa cutoff (Millipore) centrifuged at 3,000 × g and further purified by a HiLoad Superdex 200 (GE Healthcare) column in Tris-HCl buffer (10 mM Tris-HCl, pH 7.4, 0.15 M KCl, 20% glycerol, 1 mM TCEP). The pure protein was sterile-filtered through a 22 μm PVDF membrane (Millipore), and the proteins were quantified using the Reducing Agent Compatible Bicinchoninic acid assay (Pierce Biotechnology), snap-frozen in liquid nitrogen, and stored in aliquots at −80°C.

In vitro transcription of gRNA

Linear DNA fragments containing the T7 RNA polymerase promoter sequence upstream of the desired 20 bp gRNA protospacer and the gRNA backbone were generated by PCR (Q5 Hot Start MasterMix, New England Biolabs) using the appropriate forward and reverse primers (Table S1) and were concentrated on MinElute columns (QIAGEN). The gRNA was transcribed with the HiScribe T7 High Yield RNA Synthesis Kit (New England Biolabs) at 37°C for 14–16 h with 150-400 ng of linear template per 20 μl reaction.

gRNA was purified using the MEGAClear Transcription Clean Up Kit (Thermo Fisher) according to the manufacturer's instructions. Purified gRNAs were stored in aliquots at −80°C.

Fluorescence polarization (FP) assay

The fluorescence polarization assay was performed in a 384-well plate (Corning 3575) format using a total reaction volume of 30 μL. A 58-base-pair *ds*DNA with a FITC-label (λ_{ex} 490nm; λ_{em} 525nm) at the 3′ end and 12 PAM (NGG) sequences distributed throughout its length was used as the DNA template (Table S1). A 25-nM, FITC-labeled, 12PAM DNA was titrated against increasing concentrations of the SpCas9:gRNA (1:1.2) complex in a 20 mM tris(hydroxymethyl)-aminomethane (Tris)–HCl buffer (150 mM KCl, 5 mM $MgCl_2$, 1 mM DTT, pH 7.5). The fluorescence polarization signal was measured using a microplate reader (PerkinElmer, EnVision). Error bars represent ± standard deviation (s.d.) across technical replicates (n = 3).

The Z'-factor for the FP-assay was calculated using the equation

$$Z' = 1 - (3(\sigma_1 + \sigma_2))/(|\mu_1 - \mu_2|), \quad \text{(Equation 1)}$$

where σ_1 and σ_2 are the standard deviations of the DMSO control population and the SpCas9:gRNA control population, respectively, and μ_1 and μ_2 are the mean FP for the DMSO controls and SpCas9:gRNA controls, respectively.

Fluorescence polarization competition assay

In a 384-well plate (Corning 3575), 25 nM of FITC-labeled 12PAM DNA was incubated with 50 nM of the SpCas9:gRNA (1:1.2) complex in the presence and absence of unlabeled DNA (Table S1) in excess (10- and 50-fold) in a 20 mM Tris-HCl buffer (150 mM KCl, 5 mM $MgCl_2$, 1 mM DTT, pH 7.5). FP was measured using a microplate reader (PerkinElmer, EnVision). The number of PAM sequences in the unlabeled competitor DNA was varied from 0, 4, 8, and 12. Error bars represent ± s.d. across technical replicates (n = 3).

Differential scanning fluorimetry (DSF)

Protein-melting experiments were performed in a 384-well format using a 6 μL reaction volume in a LightCycler 480 instrument. A 1 μM solution of SpCas9:gRNA (1:1.2) was incubated with DNA (2 μM) at different PAM densities (0, 4, 8, and 12; Table S4) for 15 min in a 20 mM Tris-HCl buffer (150 mM KCl, 5 mM $MgCl_2$, 1 mM DTT, pH 7.5). Next, 1 μL of 100 × SYPRO Orange (Invitrogen) was added before running the melting cycle with a temperature gradient of 4.8°C/min. Experiments were performed in triplicate, and data were processed using the Roche LightCycler 480 Protein Melting software. Error bars represent ± s.d. across technical replicates (n = 4).

Bio-layer interferometry (BLI)

DNA-SpCas9 interactions were probed using BLI experiments in an Octet Red384 (Pall ForteBio) instrument. Experiments were performed in a 96-well format with a reaction volume of 180 μL using biotinylated *ds*DNA and streptavidin sensors. Next, 300 nM of biotinylated DNA with different PAM densities (0, 2, 4, and 8, Table S1) were loaded onto the sensors for 180 s in a 20 mM Tris buffer (100 mM KCl, 5 mM $MgCl_2$, 1 mM DTT, 0.01% Tween, 50 μg/mL heparin, pH 7.5). Excess DNA was washed off for 60 s using reaction buffer followed by association with 200 nM of SpCas9:gRNA (1:1.2) for 300 s. The complex was then allowed to dissociate for 3,600 s in the reaction buffer. Response curves were normalized against the reference sensor without SpCas9:gRNA.

mKate2-disruption assay

Approximately 8,000 cells/well were seeded into a 96-well plate 24 h before transient transfection with 100 ng of either CgRNA (Addgene Plasmid #64955) or T1gRNA (Addgene Plasmid #62717) plasmids using Lipofectamine 2000 (Life Technologies). Transfected cells were allowed to grow in the indicated amount of small molecule or DMSO for 24 h. Cells were then fixed using 4% paraformaldehyde and were imaged with the HCS NuclearMask Blue Stain (Life Technologies) as the nuclear counter-staining agent. Imaging was performed with an ImageXpress Micro automated microscope (Molecular Devices) at 20 × magnification under two excitation channels (blue and red) with nine acquisition sites per well. Images were analyzed using the MetaXpress software to determine the percent of mKate2-positive cells, and data were plotted using GraphPad Prism 6. The Z'-value was calculated from Equation 1 where σ_1 and σ_2 represent the standard deviations of CgRNA-transfected wells and T1gRNA-transfected wells, respectively, and μ_1 and μ_2 represent the mean $\%RFP^+$ cell population for CgRNA-transfected wells and T1gRNA-transfected wells, respectively.

Non-homologous end joining (NHEJ) assay

Approximately 8,000 cells/well were seeded in a 96-well plate 24 h before transient transfection with a total of 100 ng of DN66 (mCherry-TAG-GFP reporter) and DN78 (SpCas9 and gRNA) plasmids (1:1) using Lipofectamine 2000 (Life Technologies). Transfected cells were incubated with the indicated amount of small molecule or DMSO for 24 h. Cells were then fixed using 4% paraformaldehyde and imaged with the HCS NuclearMask Blue Stain (Life Technologies) as the nuclear counter-staining agent. Imaging was performed with an ImageXpress Micro automated microscope (Molecular Devices) at 4 × magnification under three excitation channels (blue, green, and red) with nine acquisition sites per well. Images were analyzed in the MetaXpress software to determine the

percent of NHEJ, and the data were plotted using GraphPad Prism 6. The Z'-value was calculated from Equation 1, where σ_1 and σ_2 represent the standard deviations of DN66-transfected wells and (DN66+DN78)-transfected wells, respectively, and μ_1 and μ_2 represent the mean %GFP$^-$ cell population for DN66-transfected wells and (DN66+DN78)-transfected wells, respectively.

Primary assay for compound screening

The compound library screening was performed in two steps. Initially, the DOS informer set was screened in the FP-based assay to identify the libraries enriched for hits. Then, the specific enriched libraries were also screened at greater depth using the same assay. The screening assay was performed in a 384-well plate format with a total reaction volume of 30 μL. Initially, 25 μL of 60 nM of SpCas9 was transferred to all wells of the 384-well plate except for the positive controls. Then, 25 μL of a solution containing 60 nM of SpCas9 and 300 nM of unlabeled 12PAM DNA was transferred to the positive-control wells. In the next step, 25 nL of DMSO alone or 10 mM of compounds in DMSO were transferred to the reaction mixture and incubated for 30 min at room temperature. Next, a 5 μL solution containing 360 nM of gRNA and 150 nM of FAM-labeled 12PAM DNA was added and incubated for 15 min at room temperature before measuring the fluorescence polarization signal with a microplate reader (Envision, PerkinElmer). Compounds were screened in duplicate, data were processed to calculate the Z-score $((x-\mu)/\sigma)$ values, and the values were plotted using the Spotfire analysis software (TIBCO). Hit compounds (Z-score > 3) were clustered according to the class of compound, and a hit-rate plot was generated. Entire specific libraries of the enriched compounds were then screened in the same FP assay.

Counter-screening assay

Counter-screening was performed in a similar format as the compound-screening assay. In a 384-well plate, 30 μL of 25 nM FAM-labeled 12PAM DNA was transferred to each well. Next, 25 nL of either DMSO or compound in DMSO were transferred and incubated for 30 min before measuring fluorescence polarization signal with a microplate reader (Envision, PerkinElmer). The change in the FP signal was calculated in percentile and plotted against the average Z-score values of the compounds obtained from the original compound-screening assay. Compounds that resulted in a > 3σ change in the primary assay but did not alter the FP signal by > 10% in the counter-screen assay were selected as hits. A structure-based similarity search was also performed, and compounds with a > 0.8 Tanimoto similarity using ECFP6 fingerprints were included in the hit list.

Compound–SpCas9 interaction in BLI

The experiments were performed in a 96-well format with a 180 μL reaction volume using BRD3539 and streptavidin sensors. To start, 1 μM of the biotinylated compound was loaded onto the sensors for 180 s in a 20 mM Tris buffer (100 mM KCl, 5 mM $MgCl_2$, 1 mM DTT, 0.01% Tween, pH 7.4). Compound-loaded sensors were then allowed to associate with different concentrations of the SpCas9:gRNA complex (0.15–1 μM) for 300 s followed by dissociation in reaction buffer. The reference sensor was loaded with compound and allowed to associate and dissociate in reaction buffer alone. Response curves were fitted with a 2:1 stoichiometric model, and a global fit steady-state analysis was performed using the manufacturer's protocol. Experiments were performed in triplicate.

Competition experiments were performed using a biotin-linker fragment (Figures S2D and S2E). In this experiment, streptavidin sensors were pre-incubated with 10 μM of biotin-linker for 10 min before dipping them into a solution of either 1 μM of BRD7087-biotin (Figures S2D and S2E) or reaction buffer alone. The sensors were then allowed to associate with different concentrations of SpCas9:gRNA complex (0.15–1 μM) or buffer alone.

NMR binding assay

All samples were prepared with 50 μM of BRD7087 in a 20 mM Tris buffer (pH 7.4) with varying concentrations of SpCas9:gRNA in a 3 mm NMR tube. Experiments were performed on a 600 MHz (^{19}F: 564.71 MHz) Bruker AVANCE III NMR spectrometer equipped with a 5 mm QCI-F CryoProbe and a SampleJet for automated sample handling. To acquire the spectra, a standard one-pulse ^{19}F experiment with WALTZ-16 for proton decoupling during acquisition, a 5 s recycle delay, and 256 scans were used. All spectra were recorded at 280 K. NMR data were apodized with a 1-Hz exponential function prior to Fourier transformation. All spectra were baseline corrected, and peak widths and intensities were extracted using the automated line-fitting feature provided with the MNova software package.

SpCas9 nuclease activity in eGFP-disruption assay

Approximately 200,000 U2OS.eGFP-PEST cells were nucleofected following two different methods: either by nucleofecting plasmids or by ribonucleoprotein (RNP) using the SE Cell Line 4D-Nucleofector X Kit (Lonza) according to the manufacturer's protocol. In the plasmid nucleofection method, cells were nucleofected with either 440 ng of SpCas9 (Addgene Plasmid #43861) or 400 ng of SpCas9 with 40 ng of gRNA (pFYF1320 eGFP Site#1, Addgene Plasmid #47511). Cells nucleofected only with SpCas9-expressing plasmid were used as the transfection control. In the RNP-nucleofection method, either 20 mmol of SpCas9 or 20 pmol of preformed SpCas9:gRNA (eGFP Site#1) complex were nucleofected. Approximately 20,000 transfected cells/well were plated in four replicates in a 96-well plate (Corning 3904). Cells were incubated with the indicated amount of compound or DMSO for 24 h post transfection. A DMSO solution of the compound (20 mM) was resuspended in the 10% FBS-containing growth media and thoroughly mixed before adding to the cells. Cells were then fixed using 4% paraformaldehyde and imaged with the HCS NuclearMask Blue Stain (Life Technologies) as the nuclear counter-staining agent. Imaging was performed with an ImageXpress Micro automated microscope

(Molecular Devices) at 10 × magnification under three excitation channels (blue, green, and red) acquiring nine sites per well. Images were analyzed using the MetaXpress software and data were plotted using GraphPad Prism 6.

The Z'-value was calculated using Equation 1, where σ_1 and σ_2 represent the standard deviations of the DMSO control and SpCas9:gRNA control, respectively, and μ_1 and μ_2 represent the mean %GFP$^-$ cell population for the DMSO control and SpCas9:gRNA control, respectively.

Western blot analysis

U2OS.eGFP.PEST cells stably expressing eGFP were treated with the small molecules for 24 h at 37°C prior to harvesting the cells. Cell suspensions were centrifuged at 1,000 × g for 5 min, and cells were resuspended in radioimmunoprecipitation assay (RIPA) total cell lysis buffer (Abcam) and were incubated at 4°C for 10 min. The cell suspensions were then vortexed for 10 min at 4°C followed by centrifugation at 16,000 × g for 15 min at 4°C. The supernatant was transferred to a fresh tube and processed for western blotting. Western blotting was performed following SDS-PAGE gel electrophoresis. In a typical experimental protocol, 40 μg of normalized proteins were electrophoresed on a 4%–12% Bis/Tris gel. The protein bands were transferred to a polyvinylidene difluoride (PVDF) membrane and probed with primary anti-GFP antibody (Cell Signaling #2956). Anti-actin antibody (Sigma) was used as a protein loading control.

Base-editing experiments

BE3 expression and purification

BE3 was expressed and purified as previously reported (Rees et al., 2017). BL21 Star (DE3)-competent *E. coli* cells were transformed with plasmids encoding the bacterial-codon-optimized base editor with a His_6 N-terminal purification tag. A single colony was grown overnight in 2xYT broth containing 50 μg ml^{-1} of kanamycin at 37°C. The cells were diluted 1:400 into 4 L of the same media and grown at 37°C until the OD_{600} = 0.70–0.75. The cultures were incubated on ice for 3 h, and protein expression was induced with 1 mM of isopropyl-β-D-1-thiogalactopyranoside (GoldBio). Expression was sustained for 16–18 h with shaking at 18°C. The subsequent purification steps were carried out at 4°C. Cells were collected by centrifugation and resuspended in cell-collection buffer (100 mM Tris-HCl, pH 8.0, 1 M NaCl, 20% glycerol, 5 mM tris[2- carboxyethyl]phosphine [TCEP; GoldBio], 0.4 mM phenylmethane sulfonyl fluoride [Sigma-Aldrich], and 1 EDTA-free protease inhibitor pellet [Roche]). Cells were lysed by sonication (6 min total, 3 s on, 3 s off), and the lysate was cleared by centrifugation at 25,000 × g (20 min).

The cleared lysate was incubated with His-Pur nickel-nitriloacetic acid (nickel-NTA) resin with rotation at 4°C for 90 min. The resin was washed twice with 15 column volumes of cell-collection buffer before the bound protein was eluted with elution buffer (100 mM Tris-HCl, pH 8.0, 0.5 M NaCl, 20% glycerol, 5 mM TCEP, 200 mM imidazole). The resulting protein fraction was further purified on a 5 ml Hi-Trap HP SP (GE Healthcare) cation exchange column using an Akta Pure FPLC. Protein-containing fractions were concentrated using a column with a 100 kDa cutoff (Millipore) centrifuged at 3,000 × g, and the concentrated solution was sterile-filtered through a 22 μm PVDF membrane (Millipore). After sterile filtration, the proteins were quantified using the Reducing Agent Compatible Bicinchoninic acid assay (Pierce Biotechnology), snap-frozen in liquid nitrogen, and stored in aliquots at −80°C.

Analysis of base-edited sequences

Nucleotide frequencies were analyzed using a previously described MATLAB script (Komor et al., 2017). Briefly, the reads were aligned to the reference sequence via the Smith-Waterman algorithm. Base calls with Q-scores below 30 were replaced with a placeholder nucleotide (N). This quality threshold results in nucleotide frequencies with an expected theoretical error rate of 1 in 1,000. To distinguish small-molecule-induced inhibition of C→T editing from artifactual C→T editing, we compared the sequencing reads from cells treated with the base-editor in the presence of the small molecule to the sequencing reads from base-edited cells not exposed to the small molecule. A Student's two-tailed t test was used to determine if the small-molecule-induced inhibition of C→T editing was statistically significant, with $p < 0.05$ as the threshold.

Protein transfection of base-editor BE3 into HEK293T cells

HEK293T cells were seeded on 48-well BioCoat poly-D-lysine plates (Corning) in 250 μL of antibiotic-free medium and were transfected at ~70% confluency. Prior to protein transfection, the cells were incubated with BRD7087 or BRD5779 at the indicated concentrations for 2–3 h. BE3 protein was incubated with a 1.1 × molar excess of EMX1-targeting gRNA at a final concentration ratio of 200 nM:220 nM (based on a total well volume of 275 μL). The complex was mixed with the small molecules for five minutes, incubated with 1.5 μL of Lipofectamine 2000 (Thermo Fisher), and transfected according to the manufacturer's protocol for plasmid delivery. The cells and ribonucleoprotein complex were incubated with compounds at final concentrations of 1.25 μM, 2.5 μM, 5 μM, 10 μM, or 20 μM.

Purifications and sequencing of genomic DNA

Transfected cells were harvested after 72 h in 50 μL of lysis buffer (10 mM Tris-HCl pH 8.0, 0.05% SDS, 25 μg/mL proteinase K) and incubated at 37°C for 1 h. Cell lysates were heated at 85°C for 15 min to denature proteinase K. For the first PCR, genomic DNA was amplified to the top of the linear range using Phusion Hot Start II DNA polymerase (New England Biolabs) according to the manufacturer's instructions. For all amplicons, the PCR protocol used an initial heating step of 1 min at 98°C followed by an optimized number of amplification cycles (10 s at 98°C, 20 s at 68°C, 15 s at 72°C). qPCR was performed to determine the optimal number of cycles for each amplicon. Amplified DNA was purified using RapidTip2 (Diffinity Genomics) and was barcoded with a subsequent PCR. Sequencing adapters and dual-barcoding sequences are based on the TruSeq Indexing Adapters (Illumina). Barcoded

samples were pooled and purified by gel extraction (QIAGEN) before quantification using the Qubit *ds*DNA HS Kit (Thermo Fisher) and qPCR kit (KAPA BioSystems) according to the manufacturer's instructions. The sequencing of pooled samples was performed using a single-end read from 260–300 bases (MiSeq, Illumina) according to the manufacturer's instructions.

Transcription activation experiments

The plasmid for guide-RNA targeting the *HBG1* gene was constructed by cloning a 20-nucleotide-long spacer sequence into the gRNA (MS2) cloning backbone plasmid (Addgene #61424) using the Golden Gate cloning protocol (Konermann et al., 2015). Briefly, 10 μM of the forward and reverse oligonucleotides (5′-CACCGGGCAAGGCTGGCCAACCCAT-3′ and 5′-AAACATGGGTTGGC CAGCCTTGCC-3′, respectively) were phosphorylated and annealed in the presence of T4 ligase buffer (NEB) and T4 PNK (NEB) in a thermal cycler using the following conditions: 37°C for 30 min, 95°C for 5 min followed ramping to 25°C at 5°C/min. The annealed oligonucleotides were then mixed with the gRNA (MS2) backbone and digested using the restriction enzyme *BbsI* (Fermentas FD) and ligated using T7 ligase (Enzymatics) in a thermal cycler using the following conditions: 37°C for 5 min, 20°C for 5 min, repeated for 15 cycles. Then, 2 μL of the Golden Gate reaction was transformed into DH5 alpha cells (NEB) and plated on ampicillin-containing LB plates. Plasmids were extracted and sequenced to confirm the cloning of the spacer into the gRNA (MS2) backbone.

For data reported in Figures 5J, S5G, and S5H, HEK293FT cells were maintained in high glucose DMEM with glutamax (Life Technologies) supplemented with 10% FBS (Life Technologies), 1% penicillin-streptomycin (Life Technologies), and 1 mM of sodium pyruvate (Life Technologies)(Nguyen et al., 2016). For transcription activation experiments, 20,000 cells/well were plated in a poly-D-lysine-coated 96-well plate. The cells were transiently transfected with a 1:1:1 mass ratio of the dCas9 plasmid, MS2-P65-HSF1 effector plasmid, and the gRNA plasmid targeting the *HBG1* gene or an RFP control plasmid. A total of 0.3 μg of plasmid DNA was transfected using Lipofectamine 2000 (Life Technologies) according to the manufacturer's protocol. Immediately after transfection, the cells were treated with an appropriate dose of the small-molecule inhibitors. A DMSO solution of each compound (20 mM) was resuspended in the 10%-FBS-containing growth media and thoroughly mixed before adding to the cells. After 48 h, the cells were lysed, and 5 μL of the cell lysate was used to perform reverse transcription using the RevertAid RT Reverse Transcription Kit (Thermo Fischer Scientific) as described by Joung J. et al. qPCR reactions were performed to quantify RNA expression using the TaqMan probes (Life Technologies, HBG1/HBG2: Hs00361131_g1, ACTB: Hs01060665_g1) and TaqMan Fast Advanced Master Mix (Life Technologies) in 5 μL multiplexed reactions in a 384-well format using the LightCycler 480 Instrument II (Roche). For each sample, eight technical replicates were performed. Data were analyzed using the LightCycler 480 software (Roche) using the $\Delta\Delta C_t$ method: C_t values for the gene of interest (*HBG1*) were normalized to C_t values for the housekeeping gene (*ACTB*), and fold changes in the expression level of the gene of interest were normalized to RFP-transfected control values. The data is reported as the mean ± the standard error of the mean (SEM) for technical replicates.

For data reported in Figures 2G and S2R, 250,000 cells/well were plated in a 12 well plate. The cells were transiently transfected with a 1:1:1 mass ratio of the dCas9 plasmid, MS2-P65-HSF1 effector plasmid and the sgRNA plasmid targeting the *HBG1* gene or an RFP control plasmid. A total of 1.6 μg plasmid DNA was transfected using Lipofectamine 2000 (Life Technologies) according to manufacturer's protocol. Immediately after transfection, the cells were treated with an appropriate dose of the small molecule inhibitors for 48 hours following which the cells were harvested and RNA was extracted using the EZNA Total RNA kit I (Omega) as per manufacturer's instructions. 1 μg total cellular RNA was used to perform reverse transcription using the High-Capacity cDNA Reverse Transcription Kit (Applied Biosystems) or the qScript cDNA Synthesis Kit (QuantaBio). qPCR reactions were performed to quantify RNA expression using the TaqMan probes (Life Technologies, HBG1/HBG2: Hs00361131_g1 and ACTB: Hs01060665_g1) and TaqMan Fast Advanced Master Mix (Life Technologies) in 5 μL multiplexed reactions and 384-well format using the LightCycler 480 Instrument II (Roche). For each sample, six technical replicates were performed. Data were analyzed using the LightCycler 480 software (Roche) by the $\Delta\Delta C_t$ method: C_t values for the gene of interest (*HBG1*) were normalized to C_t values for the housekeeping gene (*ACTB*) and fold-changes in the expression level of the gene of interest were normalized to RFP-transfected control. The data are reported as mean ± SEM for technical replicates.

HiBiT assay

The plasmid for guide-RNA targeting the C terminus of *GAPDH* gene was constructed by cloning a 20-nucleotide-long spacer into the SpCas9 gRNA backbone plasmid (BPK1520, Addgene # 65777) (Kleinstiver et al., 2015b). Briefly, 10 μM of the forward and reverse oligonucleotides (5′-CACCGGTCCAGGGGTCTTACTCCT-3′ and 5′-AAACAGGAGTAAGACCCCTGGACC-3′, respectively) were phosphorylated and annealed in the presence of T4 ligase buffer (NEB) and T4 PNK (NEB) in a thermal cycler using the following conditions: 37°C for 60 min, 95°C for 5 min followed by ramping to 10°C at 5°C/min. Then, 3 μg of the gRNA backbone plasmid was digested using BsmBI (NEB) and CIP (NEB) at 55°C for 16 h. The cut plasmid was isolated by gel extraction. A 0.5 μM aliquot of the annealed oligonucleotides was then ligated with 40 ng of the BsmBI-digested backbone by incubation at 24°C for 30 min in the presence of T4 DNA ligase (NEB). Finally, 5 μL of the ligation reaction was transformed into DH5 alpha cells (NEB) and plated on ampicillin-containing LB plates. Plasmids were extracted and sequenced to confirm that the spacer was cloned into the gRNA backbone.

For SpCas9 expression in cells, the previously described JDS246 plasmid was used (Kleinstiver et al., 2015b). A single-stranded oligodeoxynucleotide (ssODN) donor DNA template with the HiBiT tag was purchased as single-stranded Ultramer DNA Oligonucleotides (IDT) and resuspended to 40 μM in nuclease-free water. For the assay, 2×10^5 cells were co-transfected with 300 ng of Cas9 plasmid, 75 ng of gRNA plasmid, and 100 ng of ssODN using the DN-100 program of the 4D-Nucleofector System (Lonza) according to the manufacturer's protocols. For negative controls, either the gRNA plasmid or the ssODN was omitted. For the assay, 20,000

transfected cells were plated in each well of a 96-well plate (Corning 3904). Immediately after transfection, cells were treated with varying concentrations of BRD0539 or BRD3433 and incubated at 37°C with 5% CO_2. A DMSO solution of each compound (20 mM) was resuspended in the 10%-FBS-containing growth media and thoroughly mixed before adding to the cells. After 24 h of transfection, the cells were washed once with PBS and kept in 80 μL of PBS. An equal volume of the Nano-Glo HiBiT Lytic Reagent (Promega N3030), consisting of Nano-Glo HiBiT Lytic Buffer, Nano-Glo HiBiT Lytic Substrate, and LgBiT Protein, was added according to the manufacturer's protocol, and the cells were incubated for 10 min at ambient temperature with shaking at 600 rpm (Schwinn et al., 2018). The cells were then incubated for an additional 10 min without shaking at room temperature to allow for the HiBiT and LgBiT to equilibrate in the lysate. The lysate was then transferred to a white plate (Corning 3990), and the luminescence was measured using an Envision plate reader (Perkin-Elmer) with 1 s of integration time.

Surveyor nuclease assay

U2OS.eGFP.PEST cells were nucleofected either with either 20 pmol of SpCas9 or 20 pmol of preformed SpCas9:gRNA (EGFP Site#1) complex. Approximately 160,000 nucleofected cells/well were plated in a 12-well plate and were incubated with the indicated amount of compound or DMSO for 18 h post nucleofection. The cells were then harvested, and genomic DNA was isolated using the QuickExtract DNA extraction kit (Epicenter). Genomic DNA was subjected to PCR using primers (forward: 5′-GAGGAGCTGTT CACCGGG-3′; reverse: 5′-CTTGTACAGCTCGTCCATGC-3′) corresponding to 702 bp in the *eGFP(1)* gene segment, and the amplicons were purified using the QIAQuick PCR purification kit. The isolated amplicons were then normalized and annealed following a quick-annealing protocol (ramp 0.03°C/s). The normalized amplicons were then incubated with Surveyor nuclease S (Surveyor Mutation Detection Kits, IDT) at 42°C for 1 h. The samples were analyzed by running on a TBE gel, and the cleavage bands were visualized by staining with SYBR Gold. The inhibition of SpCas9 activity was observed by a decrease in the indel band intensity in the presence of the small molecules.

Next-generation sequencing

To start, 2×10^5 U2OS.eGFP.PEST cells were nucleofected with either 20 pmol of SpCas9 or 20 pmol of preformed SpCas9:gRNA ribonucleoprotein complex. Approximately, 1×10^6 cells per well in a 12-well format were plated in the absence or presence of the compound at the indicated concentrations in two biological replicates. Cells were harvested at 10, 12, 14, and 18 h, and genomic DNA was extracted using the QuickExtract DNA extraction solution (Epicenter) by incubating the cells at 65°C for 15 min, 68°C for 15 min, and 98°C for 10 min. Next-generation sequencing samples were prepared in a two-step PCR (Table S1) following a reported protocol. In the first step, the PCR was performed using primers that amplified the target *eGFP* genomic loci of interest and also introduced an adaptor priming sequence for the second-step PCR. The second-step PCR attached Illumina P5 adapters with barcodes, after which the PCR products were isolated via a two-step gel-purification protocol. DNA concentrations were determined using the Qubit dsDNA HS Assay Kit (Life Technologies), and sequencing of the pooled samples was performed using a single-end read from 280 bases using the MiSeq Reagent Kit v2 300 (Illumina) according to the manufacturer's protocol. The percentage of indel frequencies was calculated by analyzing the demultiplexed sequence files using MATLAB.

AcrIIA4 activity assay

The RNP was prepared by incubating SpCas9 (10 pmol) with the *eGFP*-targeting gRNA (12 pmol) for 10 min at room temperature. AcrIIA4 (50 pmol) was added to the RNP, and the mixture was incubated for 5 min at room temperature. Approximately 2×10^5 U2OS.eGFP-PEST cells were nucleofected with the RNP or RNP-AcrIIA4 mixture using the SE Cell Line 4D-Nucleofector X Kit (Lonza) according to the manufacturer's protocol. Approximately 2×10^4 transfected cells were seeded in a well of a 96-well plate (Corning 3904) and were incubated with the indicated amounts of AcrIIA4 protein for 48 h. The cells were fixed with 4% paraformaldehyde, and the nuclei were stained with HCS NuclearMask Blue Stain (Life Technologies). Imaging was performed using an ImageXpress Micro Automated High Content Microscope (Molecular Devices) at 4 × magnification under two excitation channels (blue, green) with nine acquisition sites per well. Images were analyzed using the MetaXpress software.

Reversible inhibition of SpCas9 by BRD0539

The reversal of BRD0539-mediated inhibition of SpCas9 was performed using the eGFP-disruption assay, wherein 2×10^5 U2OS.eGFP.PEST cells were nucleofected with preformed SpCas9:gRNA complex as previously described. Approximately 22,000 transfected cells/well were plated in four replicates in a 96-well plate (Corning® 3904) along with 15 μM of BRD0539 or DMSO. For AcrIIA4 reversibility experiments, a preformed SpCas9:gRNA (10 pmol) was incubated with AcrIIA4 (5 ×) for 10 min and then was nucleofected to U2OS.eGFP.PEST cells following the aforementioned protocol. The media was swapped with fresh media containing no BRD0539/AcrIIA4 at the indicated time point (2–24 h), and the cells were allowed to grow until 24 h post-nucleofection. The cells were then fixed using 4% paraformaldehyde and imaged with the HCS NuclearMask Blue Stain (Life Technologies) as the nuclear counter-staining agent. Imaging was performed with an ImageXpress Micro automated microscope (Molecular Devices) at 10 × magnification under three excitation channels (blue, green, and red) acquiring nine sites per well. Images were analyzed using MetaXpress software and data were plotted using GraphPad Prism 6.

In vitro *DNA cleavage assay*

The inhibition of SpCas9 nuclease activity was assessed in an *in vitro* DNA cleavage assay with a linearized substrate plasmid DNA. First, 94 μL of preformed SpCas9:gRNA (5.3 nM) was incubated with 3 μL of a DMSO solution of BRD0539 at the indicated concentrations (13.6−25 μM) for 30 min at room temperature followed by the addition of 3 μL of 33.3 nM substrate DNA, which was then

incubated for an additional 30 min at 37°C. The reaction was quenched by the addition of 2 μL of Proteinase K (QIAGEN) for 10 min, then was analyzed using a 1% agarose gel and visualized by SYBR Gold (Thermofisher). The bands were quantified by ImageJ and plotted in GraphPad Prism.

Plasma stability assay

The stability of the compounds in human plasma was performed following a reported protocol (Di et al., 2005). BRD0539 (5 μM) was incubated with 50% human plasma (K2 EDTA, BioreclamationIVT) in PBS for 5 h in triplicate. Eucatropine (Aldrich) and verapamil (Acros) were included as the positive and negative controls, respectively. The samples were analyzed by UPLC-MS (AB Sciex 4500 with Waters Acquity FTN) with compounds detected by SIR on a single quadrupole mass spectrometer. All integration and analysis were performed using DiscoveryQuant software.

SpCas9:gRNA binding assay

The binding of SpCas9 with gRNA was performed using a FITC-labeled crRNA:tracrRNA two-component gRNA system. FITC-labeled crRNA was mixed with an equimolar amount of tracrRNA and was annealed to form a functional gRNA. The complexation of SpCas9 with FITC-crRNA:tracrRNA was performed by titrating SpCas9 (25 nM) with increasing amounts of gRNA, which resulted in an sharp increase in the FP signal. We also confirmed the specific nature of the interaction by performing a competition experiment with unlabeled gRNA. For testing the small molecule, SpCas9 (25 nM) was incubated with different concentrations of BRD0539 (10–30 μM) for 15 min followed by the addition of FITC-labeled crRNA:tracrRNA (25 nM), and the FP signal was measured.

Disruption of SpCas9–DNA interaction by BRD0539

Protein-melting experiments were performed in a 384-well format with a 6 μL reaction volume in a LightCycler 480 instrument. For DNA binding assays, SpCas9 (1 μM) or Spcas9:gRNA (1 μM) was incubated with the indicated PAM DNA (0–12 PAM) for 15 min in a 20 mM Tris-HCl buffer (150 mM KCl, 5 mM $MgCl_2$, 1 mM DTT, pH 7.5). For inhibition assays, SpCas9 (1 μM) or Spcas9:gRNA (1 μM) was incubated with the indicated amount of either BRD0539 or the equivalent amount of DMSO for 15 min in a 20 mM Tris-HCl buffer (150 mM KCl, 5 mM $MgCl_2$, 1 mM DTT, pH 7.5). Next, a PAM DNA (2 μM) was added to each of the reactions, which were incubated for an additional 15 min followed by the addition of 1 μL of 100 × SYPRO® Orange (Invitrogen) before the melting cycle was run using a temperature gradient of 4.8°C/min. Experiments were performed in duplicate, and data were processed using the Roche LightCycler 480 Protein Melting software.

Cellular thermal shift assay (CETSA)

Approximately 1×10^6 cells pre-incubated with either DMSO or 15 μM of BRD0539 for 24 h were resuspended in PBS and transferred to 200 μL PCR tubes. The suspended cells were heated to a different temperature for 3 min and were lysed in 100 μL of RIPA buffer containing protease inhibitors at 4°C for 30 min. The clear cell lysate was collected by centrifuging the suspensions at 20,000 × g for 20 min. The supernatant was transferred to a fresh tube and processed for western blotting, which was performed using SDS-PAGE. In a typical experiment, 10 μg of proteins were electrophoresed on a 4%–12% Bis-Tris gel, and the proteins were transferred to a PVDF membrane and probed with primary anti-SpCas9 antibody (Abcam, #ab191468). The membrane was imaged, and the bands were quantified using the LI-COR Odyssey imaging system. The CETSA curves were fitted using the equation

$$y = (U\text{-}L)/(1 + e\text{^}(-(A/T\text{-}1)B)) + L, \quad \text{(Equation 2)}$$

where U and L are the upper and lower asymptotes, A is a half-way temperature, and B controls the slope of the sigmoid; the temperature T is expressed in K. After fitting, the data were re-normalized by dividing by U, and the Tm was calculated using the formula

$$T_m = AB/(B + \log(1\text{-}2L/U)). \quad \text{(Equation 3)}$$

In vitro *pulldown*

The pulldown of SpCas9 by biotinylated compound was performed by incubating the cell lysate from WM793-SpCas9 cells with streptavidin magnetic beads pre-loaded with BRD0539-biotin. Initially, a 50 μL streptavidin magnetic bead suspension was incubated with either a BRD0539-biotin conjugate or biotin-azide (20 μM) for 1 h in Tris buffer (20 mM Tris-HCl buffer, 150 mM KCl, 5 mM $MgCl_2$, 0.01% Triton, 1 mM DTT, pH 7.5). Next, the beads were collected and washed with buffer twice before being resuspended in 300 μL of 1x Cas9 activity buffer. A 100 μL aliquot of cell lysate was added to each tube along with the unlabeled BRD0539 compound (20 μM) in the competition experiment. The tubes were incubated with stirring at 4°C for 12 h before transferring the suspension to fresh tubes, and the beads were gently washed with 500 μL of 1x Cas9 activity buffer. The beads were resuspended in 1x SDS gel loading buffer (50 μL) and denatured at 98°C for 10 min. The samples were analyzed by western blotting using SDS-PAGE. In a typical experiment, 15 μL of both flow-through (FT) and eluent (E) were electrophoresed on a 4%–12% Bis-Tris gel, and the proteins were transferred to a PVDF membrane and probed with primary anti-SpCas9 antibody (Abcam, #ab191468).

Comparison of BRD0539 activity against SpCas9 and FnCpf1

To compare the specific nature of the BRD0539 inhibitory activity, we performed an eGFP-disruption assay with both SpCas9 and FnCpf1 following the aforementioned protocol. In a typical experiment, either SpCas9 or FnCpf1 plasmid (400 ng) along with their corresponding gRNA plasmid (40 ng) were nucleofected, and then the cells were incubated with the indicated amount of compound for 30 h. The cells were then processed for imaging and the quantification of eGFP-disruption.

Chemical synthesis and characterizations

Detailed methods are described in Data S1.

QUANTIFICATION AND STATISTICAL ANALYSIS

Small-molecule screening using FP and eGFP-disruption assays were performed in two replicates. The figure legends describe the number of biological replicates for various assays, which are at the least in triplicate or duplicate (BLI, HiBiT, DNA cleavage, SAR studies, and DSF). The standard deviations or standard error of the mean for these measurements were calculated using MS Excel or GraphPad Prism. Dose-dependent inhibition studies were statistically analyzed using two-tailed, unpaired t test. Unless specified otherwise, significance values are $p < 0.05$ (*), $p < 0.01$ (**), and $p < 0.001$ (***).

DATA AND SOFTWARE AVAILABILITY

Additional data related to eGFP-disruption assay, cytotoxicity, differential scanning fluorimetry, western blot, pulldown assay, NGS, and chemical characterizations of the inhibitors are available in the external repository, Mendeley Data: https://doi.org/10.17632/jpxvnh3n2t.1

Supplemental Figures

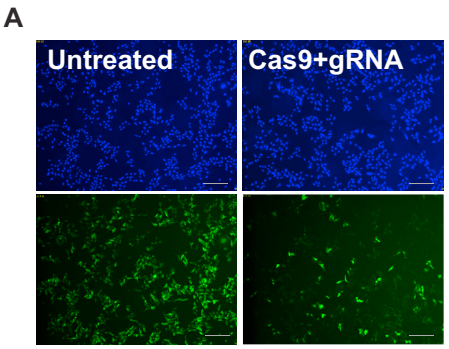

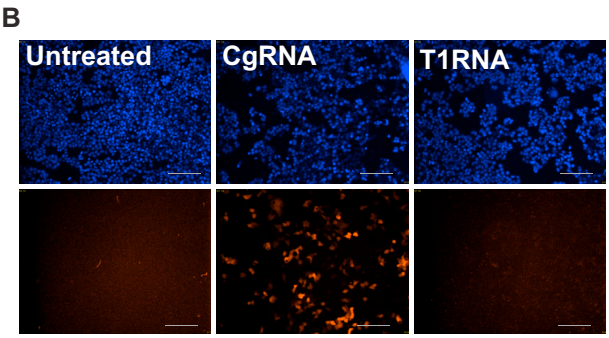

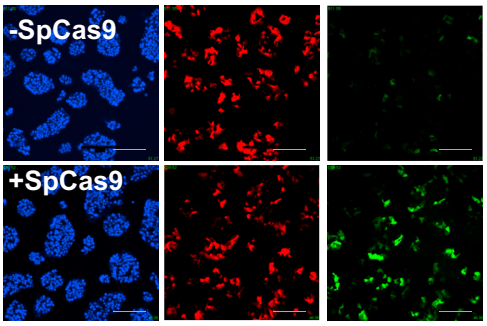

D

Assay	Z'-factor	
	96-well	384-well
eGFP-disruption	0.48	0.49
mKate2-disruption	0.37	0.36
NHEJ assay	0.32	0.46

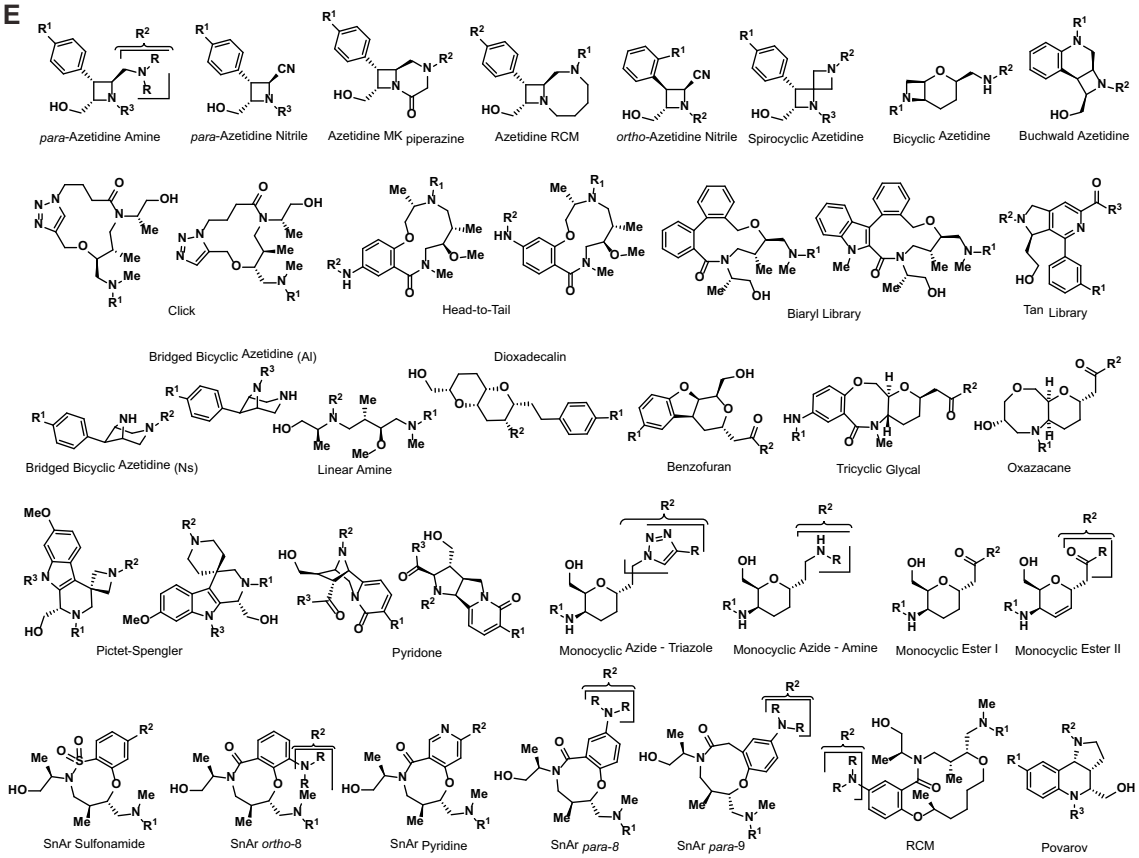

(legend on next page)

Figure S1. Chemical Structure of DOS Library and Representative Images of eGFP-Disruption Assay, mKate2-Disruption Assay, and NHEJ Assay, Related to Figures 1 and 2

(A) Representative images of the eGFP-disruption assay. U2OS.eGFP.PEST cells were nucleofected with either SpCas9 alone or SpCas9- and eGFP-targeting gRNA plasmids. Left panel shows cells nucleofected with SpCas9 alone (untreated). Right panel shows cells nucleofected with SpCas9- and eGFP-targeting gRNA expressing plasmids and treated with vehicle for 48 h. Scale bar = 200 μm.

(B) Representative images of the mKate2-disruption assay. Representative images of untreated HEK293T cells and cells transfected with T1gRNA or CgRNA. The nuclei were counter-stained with DAPI, and the expression level of mKate2 was measured using the red channel. Left, middle, and right panels represent untreated cells, cells transfected with CgRNA plasmid, and T1gRNA plasmids, respectively. Scale bar = 200 μm.

(C) Representative images of NHEJ inhibition by BRD7087. HEK293T cells were transfected with a plasmid encoding SpCas9 and gRNA and another plasmid encoding the reporter mCherry-stop codon (TAG)-GFP. The nuclei were counter-stained with DAPI and the red and green channels represent the expression levels of mCherry and GFP, respectively. Scale bar = 200 μm.

(D) Z'-factor values for cell-based secondary assays (eGFP disruption, mKate2 disruption, and NHEJ) in two different plate formats. Assays were performed in 16 technical replicates for 24 h.

(E) Structural diversity of the DOS library.

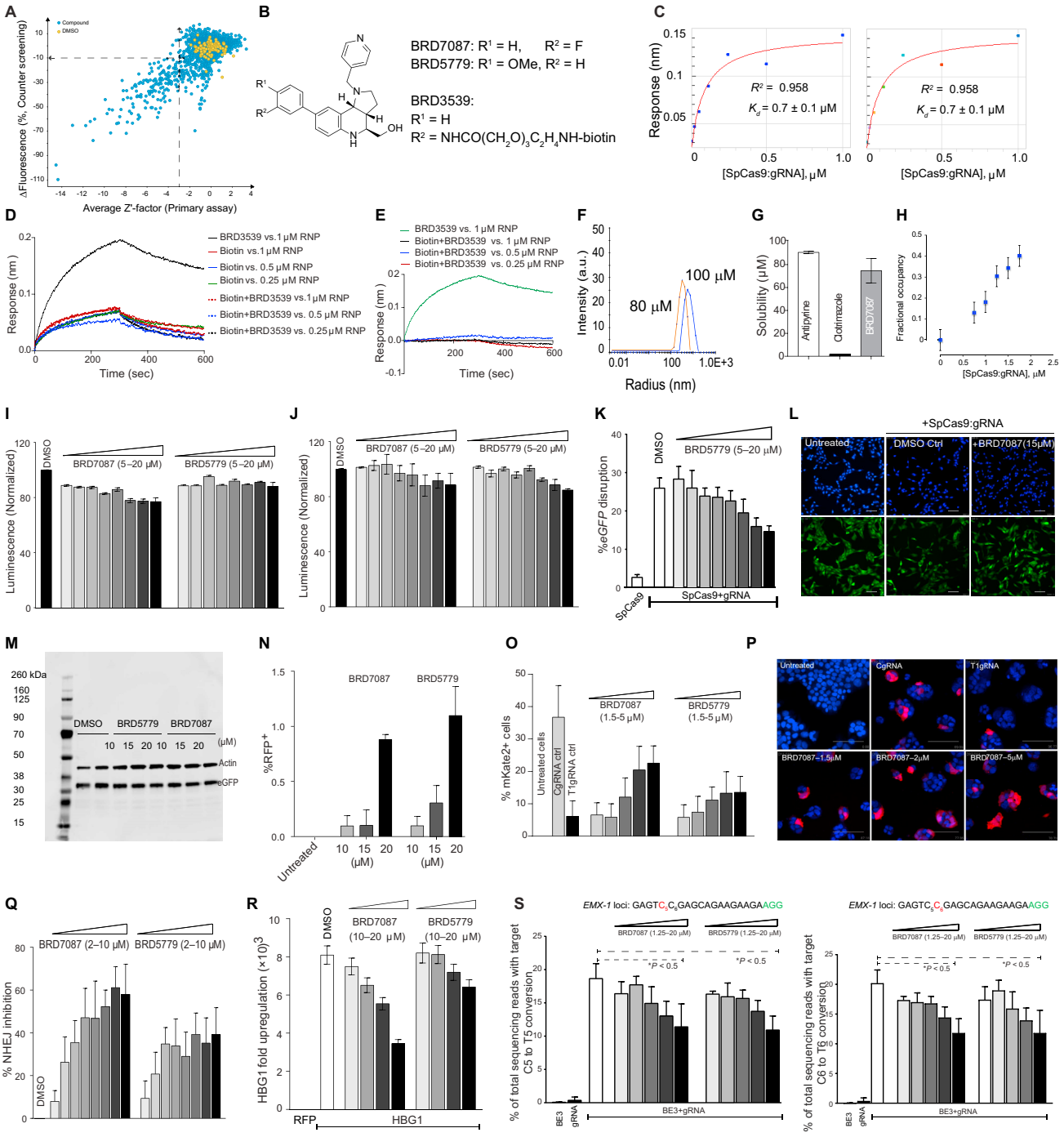

Figure S2. Biochemical and Cellular Characterization of Povarov Scaffold, Related to Figure 2

(A) Scatterplot for the primary screening assay for the Pictet-Spengler library. Dots in yellow, blue, and green represent DMSO controls, small molecules, and unlabeled 12PAM DNA competitor, respectively.

(B) Chemical structures of BRD7087, BRD5799, and BRD3539.

(C) BLI binding plots for BRD3539 and SpCas9:gRNA complex. The BLI experiment was performed using 1 μM of BRD3539 on streptavidin sensors followed by association with different concentrations of the SpCas9:gRNA complex and subsequent dissociation. Response data were plotted along the y axis, and the concentration of SpCas9:gRNA complex was plotted along the x axis. A global 2:1 (small molecule:protein) model was used to plot the steady state and determine the binding constant. The two binding plots correspond to two biological replicates.

(D) Binding competition between BRD3539 and biotin in BLI. BLI sensogram showing the interaction of streptavidin sensors loaded either with BRD3539 or biotin and SpCas9:gRNA RNP complex. BRD3539 (1 μM) or biotin (10 μM) in a 20 mM Tris buffer (pH 7.4, 100 mM KCl, 5 mM $MgCl_2$, 1 mM DTT, 0.01% Tween) was

(legend continued on next page)

loaded onto the streptavidin sensors. In the competition assay, streptavidin sensors were pre-loaded with 10 μM of biotin followed by loading 1 μM of BRD3539. The SpCas9:gRNA complex concentration was varied from 0.25–1 μM. Competitive BLI experiment with BRD3539 in the presence of 10-fold excess biotin.
(E) Background-subtracted BLI responses of BRD3539 with SpCas9:gRNA RNP complex in the presence of 10-fold excess biotin as the competitor in a 20 mM Tris buffer (pH 7.4, 100 mM KCl, 5 mM $MgCl_2$, 1 mM DTT, 0.01% Tween). The SpCas9:gRNA complex concentration was varied from 0.25–1 μM.
(F) Aggregation behavior of BRD7087. Aggregate formation for BRD7087 was determined using dynamic light scattering, between 40–100 μM in PBS. BRD7087 forms aggregates beyond 80 μM. Aggregate size distribution plots are an average of 10 individual reads. BRD7087 did not show any detectable aggregation up to ~60 μM.
(G) Determination of BRD7087 solubility in PBS. The solubility of BRD7087 in PBS was determined by mass spectroscopy after a 24 h incubation at room temperature. Antipyrine and clotrimazole are positive and negative controls, respectively.
(H) NMR binding of BRD7087 to the SpCas9:gRNA complex. ^{19}F NMR titration plot for BRD7087 with the SpCas9:gRNA complex in 20 mM Tris buffer (pH 7.4, 100 mM KCl, 5 mM $MgCl_2$, 1 mM DTT). BRD7087 (50 μM) was titrated against increasing concentrations of the SpCas9:gRNA (0.75–1.75 μM) complex.
(I) Cell viability of U2OS.eGFP.PEST cells in the presence of the small molecules. Cell viability was determined by measuring the ATP content of U2OS.eGFP.PEST cells upon incubation with BRD7087 or BRD5779 (5–20 μM) for 24 h. Error bars represent ± s.d. across technical replicates (n = 3).
(J) Cell viability of HEK293T cells in the presence of the small molecules. Cell viability was determined by measuring the ATP content of HEK293T cells upon incubation with BRD7087 or BRD5779 (5–20 μM) for 24 h. Error bars represent ± s.d. across technical replicates (n = 3).
(K) Dose-dependent inhibition of SpCas9 by BRD5779 in U2OS.eGFP.PEST cells. Compound was tested in a concentration range of 5–20 μM with a 1.2 fold dilution. U2OS.eGFP.PEST cells were nucleofected with SpCas9- and gRNA-expressing plasmids and were incubated with the indicated concentration of compound for 24 h before imaging. Error bars represent ± s.d. across technical replicates (n = 4). *$p \leq 0.0001$ for the small molecule at 20 μM compared to DMSO. (unpaired t test, two-tailed)
(L) Representative images of the eGFP-disruption assay. U2OS.eGFP.PEST cells were nucleofected with either SpCas9 alone or SpCas9- and eGFP-targeting gRNA plasmids and were treated with either the vehicle alone or the small molecule. Left panel represents cells nucleofected with SpCas9 alone. Middle panel represents cells nucleofected with SpCas9- and *eGFP*-targeting gRNA-expressing plasmids and treated with vehicle. Right panel represents cells nucleofected with SpCas9- and eGFP-targeting gRNA and treated with 15 μM of BRD7087 for 24 h. Scale bar = 100 μm.
(M) Effect of inhibitors on eGFP protein expression in U2OS.eGFP.PEST cells. The western blot analysis of eGFP protein expression in U2OS.eGFP.PEST cells was performed in the presence of DMSO and the inhibitors BRD5779 or BRD7087. Cells were incubated with either BRD5779 or BRD7087 at the indicated concentrations for 24 h before they were harvested and processed for western blotting. No change was observed in eGFP expression levels in the presence or absence of the compounds.
(N) Auto-fluorescence of U2OS.eGFP.PEST cells treated with the inhibitors in the eGFP-disruption assay. Cells were imaged in the RFP channel with the same exposure time as that used for the GFP channel in the eGFP-disruption assay. Small-molecule-treated cells showed a maximum of ~1% auto-fluorescing population, indicating no significant contribution of auto-fluorescence. Error bars represent ± s.d. across technical replicates (n = 4).
(O) Dose-dependent inhibition of SpCas9 by the inhibitors in the mKate2-disruption assay. HEK293T cells were transfected with a single plasmid encoding SpCas9, gRNA, and mKate2 (T1gRNA). Cells transfected with a plasmid encoding SpCas9, mKate2, and a non-targeting gRNA (CgRNA) were used as the positive control. Cells transfected with T1gRNA were incubated either in the presence of DMSO or the inhibitors (1.5–5 μM) for 24 h. Error bars represent ± s.d. across technical replicates (n = 3).
(P) Representative images of the mKate2-disruption assay. Representative images of untreated HEK293T cells and cells transfected with T1gRNA or CgRNA. The nuclei were counterstained with DAPI, and the expression level of mKate2 was measured using the red channel. Top panels represent untreated cells or cells transfected with the indicated plasmid and incubated with DMSO. Bottom panels represent cells transfected with T1gRNA and incubated with BRD7087 at the indicated concentrations. Scale bar = 100 μm.
(Q) Dose-dependent inhibition of SpCas9-mediated NHEJ. HEK293T cells were transfected with a plasmid encoding SpCas9, gRNA, and another plasmid encoding the reporter mCherry-Stop Codon (TAG)-GFP. Transfected cells were incubated with either DMSO or the small molecules (2–10 μM) for 24 h. Error bars represent ± s.d. across technical replicates (n = 3).
(R) Dose-dependent inhibition of dSpCas9-based transcriptional activation of the *HBG1* gene in HEK293FT cells. Cells were transfected with dSpCas9, MS2.p65.HSF1.GFP plasmids, and either the *RFP* or *HBG1* gRNA plasmid and were incubated in the presence of the small molecules at the indicated concentration for 48 h before RT-qPCR analysis. Error bars represent ± s.e.m. for technical replicates (n = 6).
(S) Dose-dependent inhibition of the SpCas9(A840H)-cytidine deaminase conjugate (BE3) targeting the *EMX1* gene in HEK293T cells. Small molecules pre-incubated with BE3:gRNA ribonucleoprotein were delivered to HEK293T cells and incubated in the presence of either DMSO or small molecules at the indicated concentration for 72 h. The cells were then harvested and processed for DNA sequencing to evaluate the extent of C5→T5 or C6→T6 conversion. Error bars represent ± s.d. across biological replicates (n = 3).

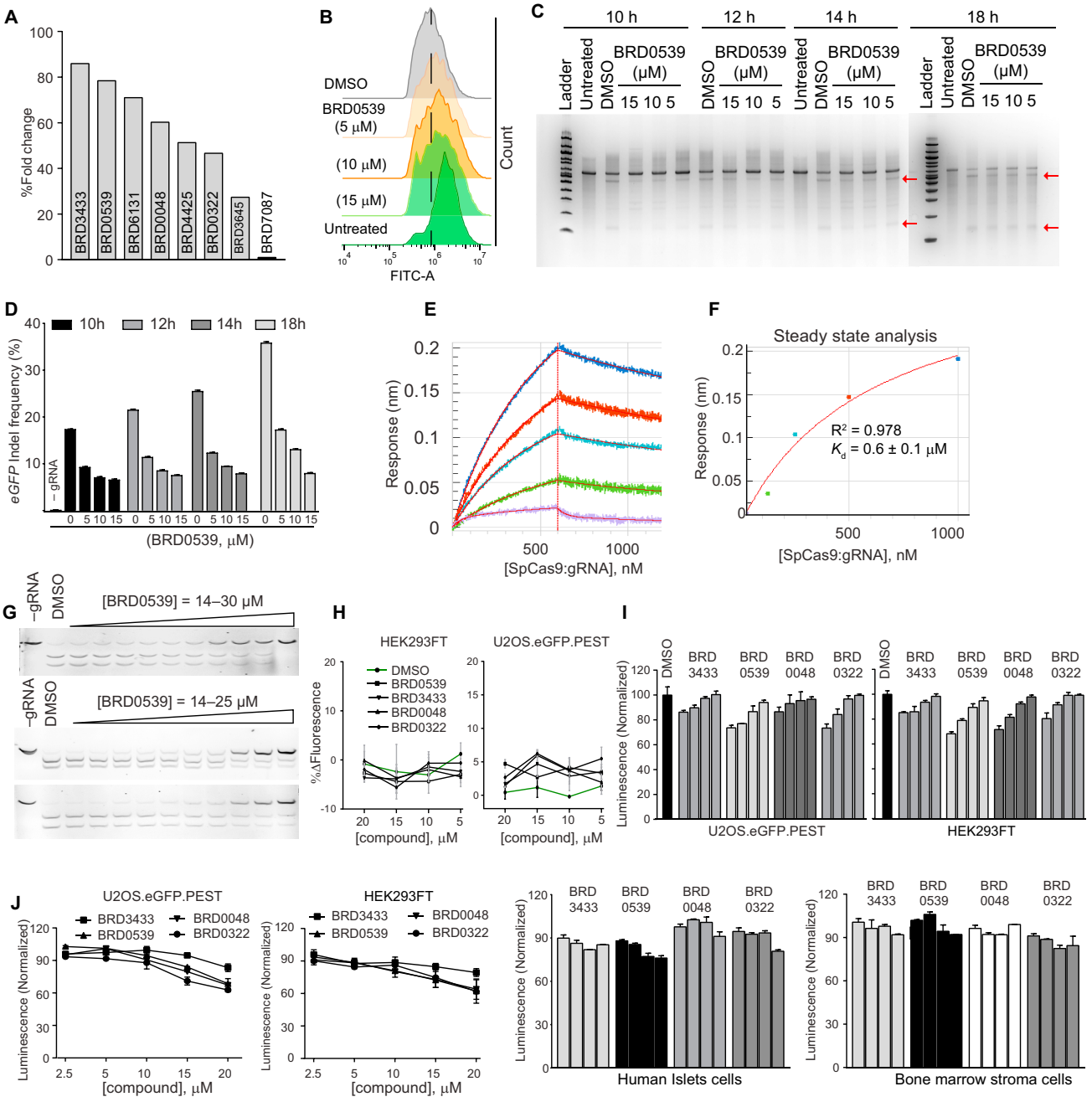

Figure S3. Biochemical and Cellular Characterization of SpCas9 Inhibitors, Related to Figure 3

(A) Inhibition of SpCas9 by BRD7087 and its analogs in U2OS.eGFP.PEST cells. Cells were nucleofected with either SpCas9 or preformed SpCas9:gRNA ribonucleoprotein complex and were incubated with 15 μM of compound for 24 h before imaging. Error bars represent ± s.d. across technical replicates (n = 4).

(B) Flow-cytometric analysis of eGFP-disruption assay. Inhibition of SpCas9 by BRD0539 in U2OS.eGFP.PEST cells. Cells were nucleofected with either SpCas9 or preformed SpCas9:gRNA ribonucleoprotein complex and were incubated with the indicated concentration of compound for 24 h before analysis.

(C) Surveyor assay analysis of the *eGFP* gene from U2OS.eGFP.PEST cells indicating inhibition of SpCas9-induced indel bands. Cells were nucleofected with either SpCas9 or preformed SpCas9:gRNA ribonucleoprotein complex and were incubated with the compound at the indicated concentration for 10, 12, 14, and 18 h before isolating the genomic DNA and analyzing it by the surveyor assay.

(D) Next-generation sequencing analysis of *eGFP* indicating dose and time-dependent inhibition of SpCas9 by BRD0539 in U2OS.eGFP.PEST cells. Cells were nucleofected with either SpCas9 or the preformed SpCas9:gRNA ribonucleoprotein complex targeting the *eGFP* gene and were incubated with BRD0539 at the indicated concentrations for 10, 12, 14, and 18 h before harvesting genomic DNA. Error bars represent ± s.d. across technical replicates (n = 2) of two biological replicates.

(legend continued on next page)

(E) BLI binding plots for BRD3433-biotin and SpCas9:gRNA complex. BLI experiment was performed using 1 μM of BRD3433-biotin on streptavidin sensors followed by association with different concentrations of the SpCas9:gRNA complex and subsequent dissociation. Response data were plotted along the y axis and the concentration of SpCas9:gRNA complex was plotted along x axis.

(F) Steady-state analysis of the BLI binding results to determine the dissociation constant. A global 2:1 (small molecule:protein) model was used to plot the steady state and determine the binding constant.

(G) Inhibition of SpCas9 by BRD0539 in a DNA cleavage assay. SpCas9:gRNA (5 nM) was incubated with BRD0539 at the indicated concentrations (14–30 μM) for 30 min at room temperature followed by the addition of substrate DNA (2,783 bp, puc57) and incubation for an additional 30 min at 37°C.

(H) Auto-fluorescence of HEK293FT and U2OS.eGFP.PEST cells treated with the inhibitors in the eGFP-disruption assay. Cells were imaged in the GFP channel with the same exposure time as that used for the *eGFP* disruption assay. Small-molecule-treated cells showed a maximum of ~5% auto-fluorescing population, indicating no significant contribution of auto-fluorescence. Error bars represent ± s.d. across technical replicates (n = 4).

(I) Cell viability of U2OS.eGFP.PEST and HEK293FT cells in the presence of the small molecules. Cell viability was determined by measuing the ATP content of U2OS.eGFP.PEST and HEK293FT cells upon incubation with the compounds (5, 10, 15, and 20 μM) for 24 h. Error bars represent ± s.d. across technical replicates (n = 3).

(J) Cell viability of U2OS.eGFP.PEST, HEK293FT, human islets, and bone marrow stroma cells in the presence of small molecules. Cell viability was determined by measuring the ATP content of human islets and bone marrow stroma cells upon incubation with the compounds (5, 10, 15, and 20 μM) for 48 h. Error bars represent ± s.d. across technical replicates (n = 3).

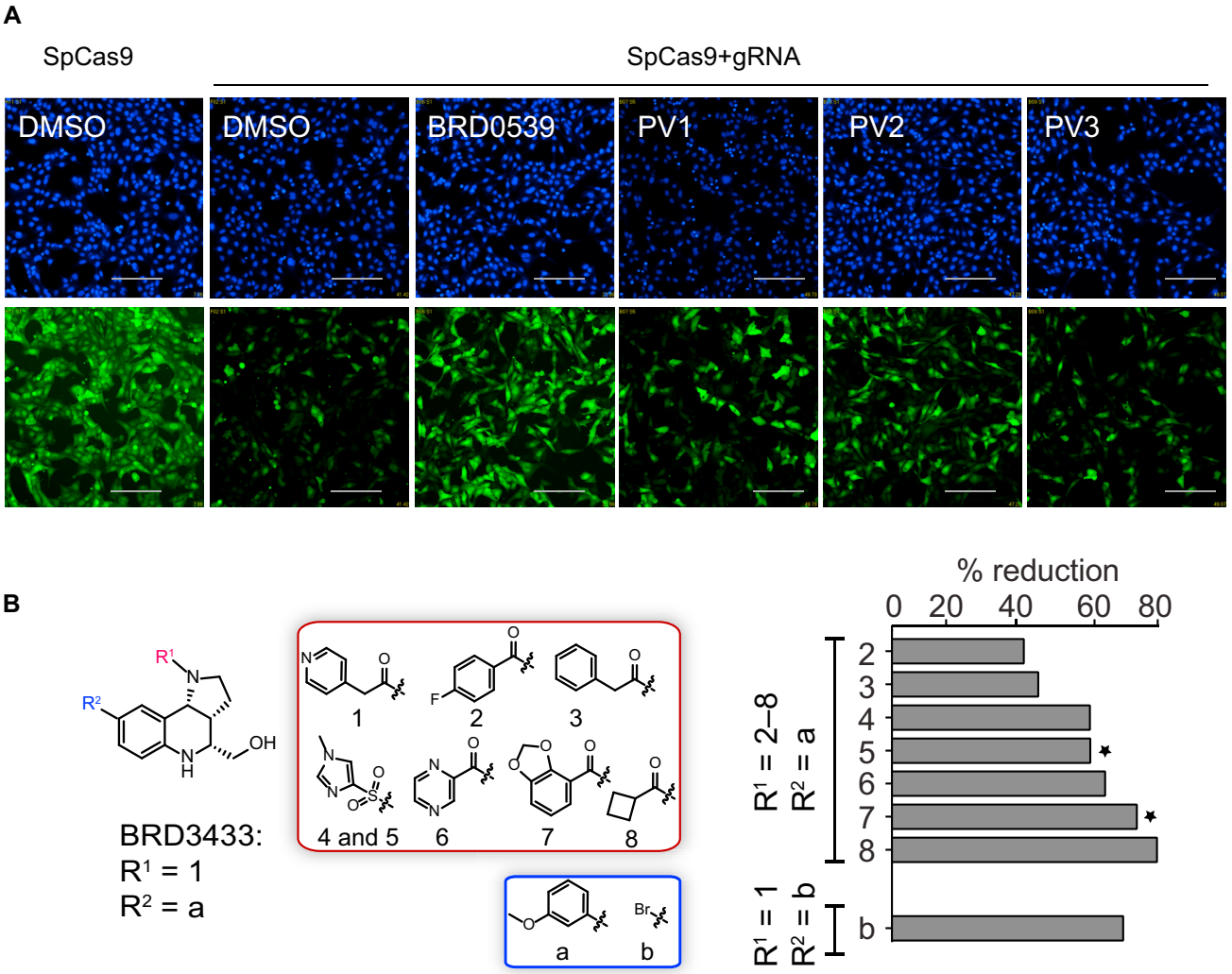

Figure S4. Structure-Activity Analysis, Related to Figure 4

(A) Representative images of the eGFP-disruption assay. U2OS.eGFP.PEST cells were nucleofected with either SpCas9 alone or preformed SpCas9:gRNA ribonucleoprotein complex and were treated with the vehicle alone or the compounds at 15 μM for 24 h. The top and bottom panels represent the DAPI and GFP channels, respectively.

(B) Structure-activity relationship studies of BRD3433 in the eGFP-disruption assay in U2OS.eGFP.PEST cells. The top set of numbered functional groups represents variation of the 1-*N*-cap position (R^1), whereas the bottom lettered set represents the functional group variation at position 8 (R^2). The bar plot depicts the reduction in the activity of the different structural analogs with respect to that of BRD3433. Asterisk-labeled compounds contain a methyl group at the 4-*N* position, while the others have a proton. The data are an average of two biological replicates.

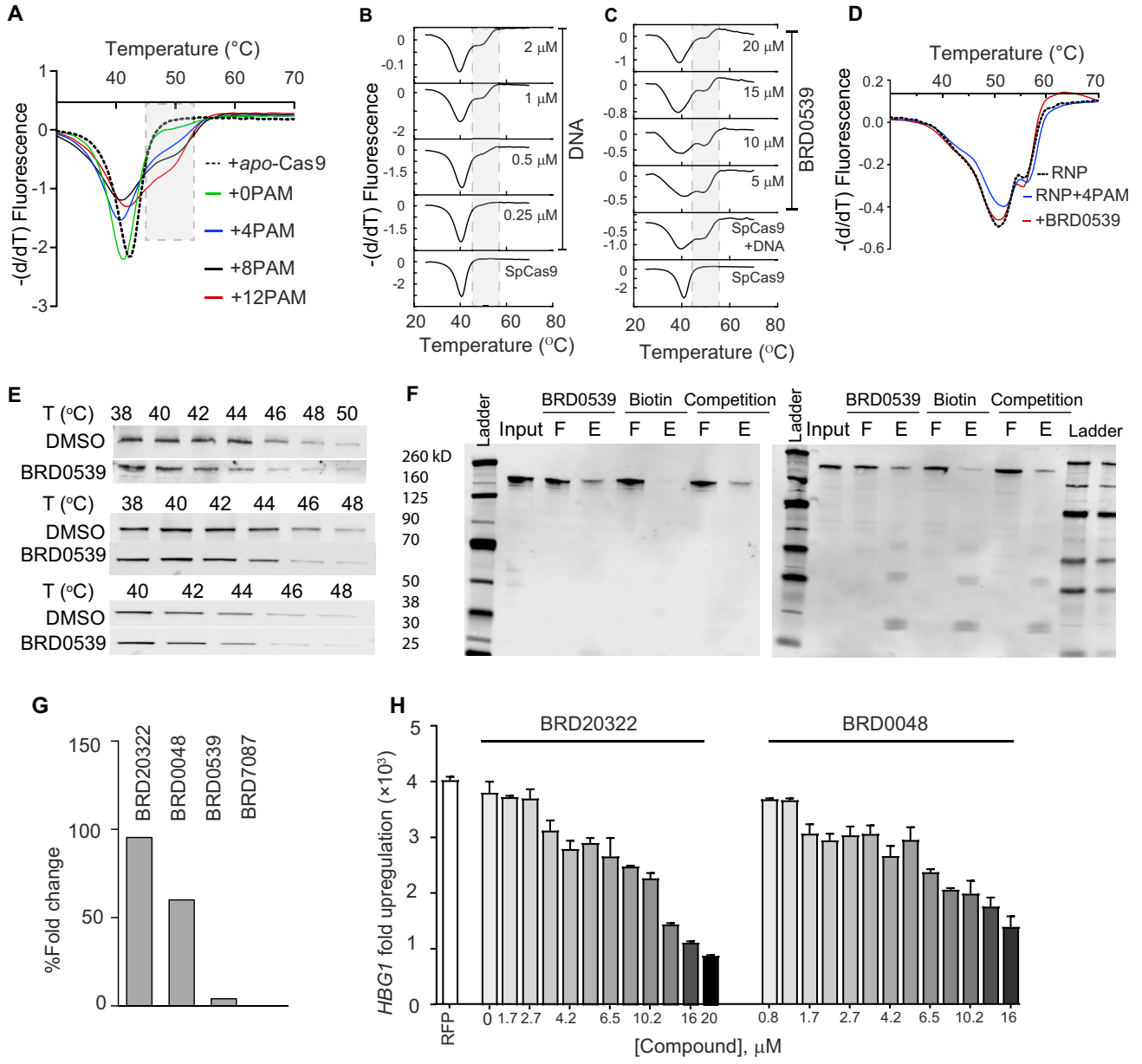

Figure S5. Mechanism of Action, Specificity, and Inhibition of dCas9-Based Transcriptional Upregulation, Related to Figure 5

(A) Biological replicate data of differential scanning fluorimetry studies of the *apo*-SpCas9 interaction with DNA. SpCas9 (1 μM) was incubated with DNA (2 μM) bearing an increasing number of PAM sequences (0–12 PAM).

(B) Differential scanning fluorimetry assay plots showing the formation of a more stable SpCas9 complex (shaded region) upon binding with the increasing concentration (0.25, 0.5, 1, and 2 μM) of 8PAM DNA. Error bars represent ± s.d. across technical replicates (n = 2).

(C) Differential scanning fluorimetryDSF assay plots depicting the destabilization of SpCas9:8PAM DNA (1 μM:2 μM) complexes (shaded region) upon incubation with an increasing concentration (5, 10, 15, and 20 μM) of BRD0539. Error bars represent ± s.d. across technical replicates (n = 2).

(D) Differential scanning fluorimetry studies showing inhibition of SpCas9:gRNA binding to 4PAM DNA by BRD0539. SpCas9:gRNA (1 μM) was incubated with 4PAM DNA (2 μM) in the presence of either DMSO or BRD0539 (20 μM). Data are for one of the two replicates.

(E) Representative immunoblots of cellular thermal shift assay (CETSA) for SpCas9 in WM793 melanoma cells in the absence or presence of BRD0539. WM793 cells stably expressing SpCas9 were incubated with 15 μM of BRD0539 for 24 h before performing the CETSA and analyzing by western blot.

(F) *In vitro* pulldown assay of SpCas9 by the BRD0539-biotin conjugate from WM793-SpCas9 cell lysate. Streptavidin magnetic beads pre-loaded with either BRD0539-biotin or biotin-azide were incubated with WM793-SpCas9 cell lysate for 12 h before processing the samples for western blotting. BRD0539 (20 μM) was used as a competitor. F and E represent flow-through and eluent, respectively.

(G) Inhibition of dSpCas9-based transcriptional upregulation of the *HBG1* gene in HEK293FT cells by BRD7087. Cells were transfected with dSpCas9, MS2.p65.HSF1.GFP plasmids, and either the *RFP* or *HBG1* gRNA plasmid and were incubated in the presence of the small molecules at the indicated

(legend continued on next page)

concentration for 48 h before RT-qPCR analysis. Data represents an average of eight technical replicates. The y axis represents %fold change in the activity of the compound with respect to BRD7087.

(H) Dose-dependent inhibition of dSpCas9-based transcriptional upregulation of the *HBG1* gene in HEK293FT cells. Cells were transfected with dSpCas9, MS2.p65.HSF1.GFP plasmids, and either the *RFP* or *HBG1* gRNA plasmid and were incubated in the presence of the small molecules at the indicated concentration for 48 h before RT-qPCR analysis. The experiments were performed in three biological replicates, and each biological replicate was processed in eight technical replicates. The data represent mean ± s.e.m. for technical replicates. *$p \leq 0.0001$ for both small molecules at 15 μM as compared to DMSO (unpaired t test, two-tailed).